Magmatic To Solid-State Evolution Of A Shallow Emplaced Agpaitic Tinguaite (The Suc De Sara Dyke, Velay Volcanic Province, France): Implications For Peralkaline Melt Segregation And Extraction In Ascending Magmas

Thomas Pereira, Laurent Arbaret, Joan Andújar, Mickaël Laumonier, Monica Spagnoli, Charles Gumiaux, Gautier Laurent, Aneta Slodczyk, Ida Di Carlo

To cite this version:

Thomas Pereira, Laurent Arbaret, Joan Andújar, Mickaël Laumonier, Monica Spagnoli, et al.. Magmatic To Solid-State Evolution Of A Shallow Emplaced Agpaitic Tinguaite (The Suc De Sara Dyke, Velay Volcanic Province, France): Implications For Peralkaline Melt Segregation And Extraction In Ascending Magmas. European Journal of Mineralogy, 2024, 36, pp.491-524. 10.5194/ejm-36-491-2024 . insu-04676498

HAL Id: insu-04676498
https://insu.hal.science/insu-04676498v1

Submitted on 26 Aug 2024

Eur. J. Mineral., 36, 491–524, 2024
https://doi.org/10.5194/ejm-36-491-2024

European Journal of
Mineralogy
Open Access

Magmatic to solid-state evolution of a shallow emplaced agpaitic tinguaite (the Suc de Sara dyke, Velay volcanic province, France): implications for peralkaline melt segregation and extraction in ascending magmas

Thomas Pereira[1], **Laurent Arbaret**[1], **Juan Andújar**[1], **Mickaël Laumonier**[2], **Monica Spagnoli**[1], **Charles Gumiaux**[1], **Gautier Laurent**[1], **Aneta Slodczyk**[1], **and Ida Di Carlo**[1]

[1]Institut des Sciences de la Terre d'Orléans, UMR 7327 (CNRS-Université Orléans-BRGM), Orléans, France
[2]Université Clermont Auvergne, CNRS, IRD, OPGC, Laboratoire Magmas et Volcans,
63000 Clermont-Ferrand, France

Correspondence: Thomas Pereira (thomas.pereira@univ-lorraine.fr) and Laurent Arbaret
(laurent.arbaret@univ-orleans.fr)

Received: 25 August 2023 – Revised: 22 March 2024 – Accepted: 27 March 2024 – Published: 25 June 2024

Abstract. In the last decades the mush model has been generalized to the complete trans-crustal magmatic system in which differentiation would be driven by segregation and extraction of trapped melts from crystal-rich mushes. Melt extraction processes involved are porous flow and strain localization, the latter being regarded as the main process acting during transfer through dykes and necks along which high differential stresses are acting on. We combine structural measurements together with petrological analyses and textural observations to constrain the model of emplacement and finally emphasize how shear deformation and strain localization structures promoted the residual melt segregation that occurred in a shallow silica-undersaturated peralkaline intrusion (Suc de Sara, Velay volcanic province, French Massif Central).

In this study, we demonstrate that segregation and subsequent extraction of the CO_2-rich residual melt occurred during magma ascent and final emplacement of the Suc de Sara tinguaite. Contrasting features of shear deformation between the margins that exhibited different permeabilities highlight that melt segregation started by compaction as a loose packing of emerging microlites and continued with melt filling of an anastomosed C/C′ band network developing in the crystal-rich mush subjected to high shear strain. Subsequent melt extraction throughout the country rock was controlled by the permeability of the hanging wall. Along the western hanging wall of the intrusion, extraction of the residual melt was prevented by the 15 cm thick chilled margin. In contrast, segregated melt circulated through the highly porous and permeable eastern margin, causing the fenitization of the country rock.

1 Introduction

In the last few decades there has been a paradigm shift in progress: instead of mostly liquid, magma bodies are now inferred to be bodies dominated by crystal-rich mush, a mix of crystals, and silicate liquid (Ward et al., 2014; Delph et al., 2017). This model of a mush zone with limited pockets of mobile magmas (Bachmann and Bergantz, 2008) has been generalized as a continuum over the entire crust from the deep ductile hot crust to the shallower chambers opened to volcanic systems, and it is called the trans-crustal magmatic system (TCMS; Cashman et al., 2017; Allan et al., 2013; Holness, 2018). In this model, the fundamental process of differentiation is driven by segregation and extraction of trapped melts from highly viscous crystal-rich mushes (Dufek and Bachmann, 2010; Burgisser and Bergantz, 2011). Melt transfer architecture arises from compaction and shear: (1) melt transfer by porous flow, where crystal network permeability is the controlling parameter (Dufek and Bachmann, 2010), and (2) melt channel formation by shear localization (Katz et al., 2006). Strain localization in crystal-rich zones is commonly observed in highly dynamic magmatic systems such as convective cells in magma chambers and hanging walls of dykes and necks along which high differential stresses are acting on (Smith, 1997; Paterson et al., 1998). While it is nearly impossible to obtain examples of a "living mush" in deeply emplaced pluton, sub-volcanic systems may preserve various stages of deformed mushes that were fossilized during rapid cooling (Geshi, 2001).

We combine structural measurements at the regional scale and along a complete cross-section of the silica-undersaturated Suc de Sara intrusion (6.5 Ma; Mergoil and Boivin, 1993), together with petrological analyses and textural observations. Thus, we better constrain the model of emplacement and finally emphasize how shear deformation and strain localization structures promoted the residual melt segregation that occurred in this differentiated intrusion during its shallow emplacement (< 150 MPa) in the Boutières graben (Mergoil and Boivin, 1993). We emphasize that melt segregation began by forming planar distribution domains in a loose stack of emerging microlites. During cooling, increasing crystal fraction led to the development of localized melt-rich shear bands. Finally, we point out the control of the contrasted permeability of the hanging wall on melt extraction throughout the country rock.

2 Geological settings

The Velay volcanic province is located in the southeast of the French Massif Central (Fig. 1a). This region is characterized by a series of N140° E directed tertiary horsts and grabens affecting the thinned granitic and migmatitic Variscan basement (Mergoil, 1968; Couzinié et al., 2014; Fig. 1b) covered by alkaline lavas from monogenetic volcanoes over the last 15 Myr.

2.1 The Velay basement

The Velay basement is composed of a set of granites and migmatites emplaced during the Westphalian (Carboniferous sub-stage) after the anatexis of a metamorphic series including prior monzogranitic, paragneiss, orthogneiss, amphibolite, and basic massifs (Dupraz and Didier, 1988; Couziné et al., 2014; Barbey et al., 2015). The formation of the Velay migmatitic complex was established in the Upper Carboniferous, at the end of the collision episode that generated the Variscan Chain, which was built during a period from the Devonian to the Carboniferous (between 400 and 300 Ma). Beneath the Velay, the crust is strongly thinned, with a thickness of about 25 km (Mergoil and Boivin, 1993, and references therein) lying above a very heterogeneous lherzolitic mantle (Berger and Vannier, 1984). Tectonically, the Velay basement is affected by large northwest–southeast faults associated with northeast–southwest faults. Particularly in the eastern Velay, the compartmentalization of the basement into horsts and grabens is controlled by two networks of regional faults almost oriented N080° E–N090° E and N140° E (Fig. 1b; Blès et al., 1989). For the period corresponding to the volcanic activity of the Velay province, the east–west Oligocene extension continued during most of the Miocene with the activation of this pair of normal fault networks (Bout, 1966; Mergoil and Boivin, 1993). At the end of the Miocene, the period for the Suc de Sara formation, a northwest–southeast compression caused the reactivation of the pre-existing fault network with mainly horizontal displacement. Finally, in the Pliocene, basaltic lava flows of the Devès are synchronous with the Velay basement extension marked by normal faults.

2.2 The Velay volcanism

From the late Oligocene to the Holocene, the Massif Central experienced two major magmatic episodes (Maury and Varet, 1980; Merle and Michon, 2001). The first episode ranging from 24 to 12 Ma was essentially expressed in the north of the French Massif Central, induced and associated with a strong crustal thinning (25 % maximum). The second episode ranging from 14 Ma to less than 10 000 years ago was characterized by the emplacement of large magmatic provinces (eastern Velay, Devès, Cantal, etc.) in the south. This major volcanic phase is contemporaneous with a general uplift with two paroxysm peaks from 9 to 6 Ma and from 3.5 to 0.5 Ma. After Malcles et al. (2020), the uplift occurred mainly in the Pliocene–Quaternary (last 4 Myr).

The volcanic massif of Velay includes three volcanic areas: the Devès, the Meygal, and the Mézenc where the Suc de Sara is located (Fig. 1a). In the eastern Velay (Fig. 1b), the volcanic formations of the Mézenc volcanic field can be separated into three distinctive episodes that are visible on the wall of the graben (Cirque des Boutières valley; Jung, 1971; Mergoil and Boivin, 1993): (1) a basal level composed of basalt flows and strombolian scoria cones; (2) above, stratified pipernoid tuffo-lavas covered by several layers of more or less differentiated basalts; (3) trachyandesite lava flows ending the sequence. This volcanism began around 13.5 Ma during a period of tectonic extension (Fig. 2a) essentially by extrusions of phonolites (Emblavès sector to the northwest) preceding the emission of subalkaline trachytes with a paroxysm around 12 to 10 Ma. In the southeast sector (Boutières graben), eruptions of differentiated lavas (phonolites, trachytes) occurred between 8.5 and 5.7 Ma (Mergoil and Boivin, 1993). The youngest eruptions (< 5 Ma) were exclusively basaltic and confined to the western Velay (Devès and Le Puy basin; Figs. 1, 2a).

The Velay volcanic province has the particularity of being composed of a continuous series from basalts to differentiated SiO_2-oversaturated and SiO_2-undersaturated products (Mergoil and Boivin, 1993). While experimental work

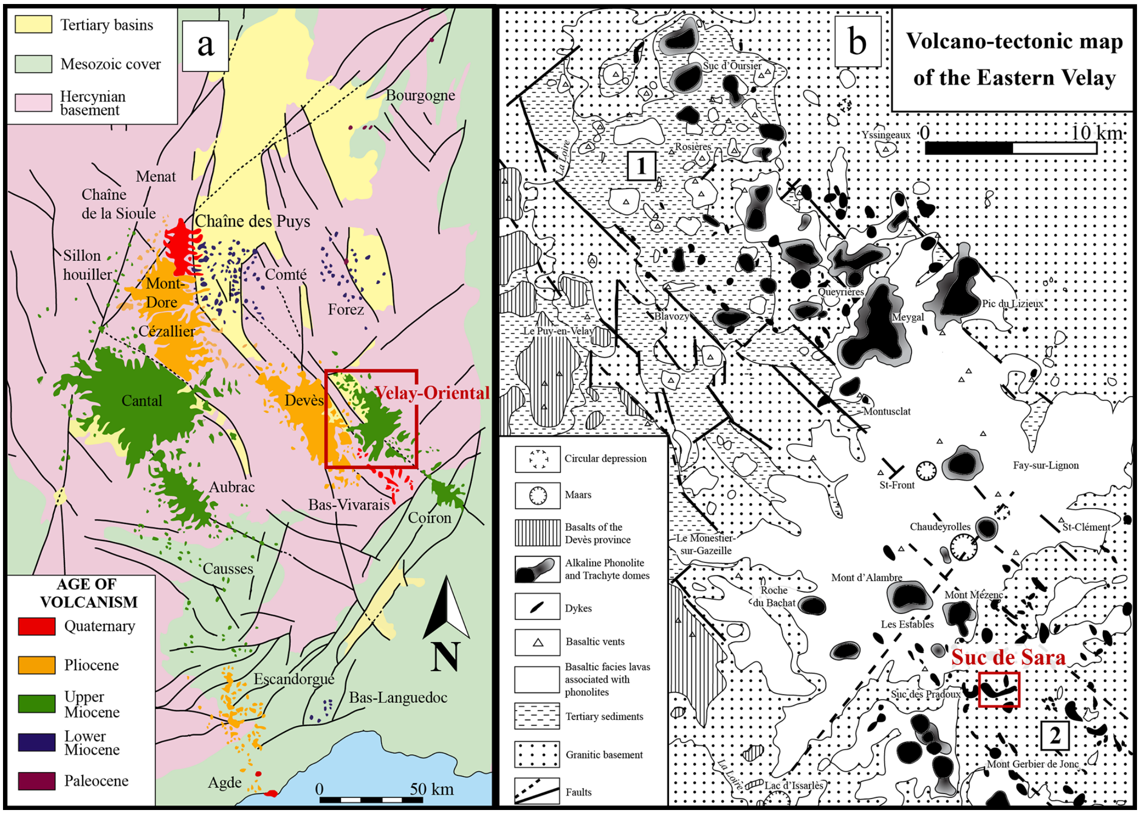

Figure 1. **(a)** Geographic positioning of the Velay volcanic province in regard to the different volcanic fields of the French Massif Central (modified from Boivin et al., 2004). The red inset represents the zoom shown in **(b)**. **(b)** Volcano-tectonic map of the eastern Velay (modified from Jung, 1971). The red inset corresponds to Fig. 3a. (1) is Emblavès graben; (2) is Boutières graben.

demonstrates that phonolitic liquids can be obtained directly by the low melting rate of peridotites (Laporte et al., 2014), differentiation to saturated, oversaturated, or undersaturated terms is generally due to crustal contamination or mineral fractionation from a basaltic or basanitic parent liquid such as alkali feldspar (Jeffery and Gertisser, 2018), plagioclase, and pyroxene (Ablay et al., 1998) or amphibole (Legendre et al., 2005). In the case of the differentiated lavas of the Velay series, the differentiation is explained by a strong fractionation of alkali feldspars, the crustal contamination remaining insignificant (Dautria et al., 2004).

For several years, miaskitic and agpaitic parageneses have been put forward to define peralkaline rocks. The distinction between the two was then based on the Na / Al–K ratio and the crystallization sequence of the various mineral phases (e.g. Batard, 1974; Hodges, 1991; Mergoil and Boivin, 1993). A recent review proposes new definitions for the terms miaskitic and agpaitic: in some cases, the extreme enrichment of alkalis, halogens (F, Cl, Br, and I), high-field-strength elements (HFSEs, such as Zr, Hf, Nb, Ta, and U), and rare earth elements (REEs) during the differentiation of peralkaline magmas may result in the precipitation of a wealth of otherwise rare minerals. The presence of these diverse and structurally complex HFSEs defines the so-called agpaitic rocks as opposed to miaskitic rocks, in which HFSEs are hosted by zircon and titanite, as is typical of most other igneous rocks (Marks and Markl, 2017). The differentiated products of the Velay are represented by trachytes and phonolites with alkalinity (Na / Al–K) ranging from 0.8 to 1.3 (Fig. 2b, c; Batard, 1974; Macdonald et al., 2021, for another recent review). Batard (1974) showed that phonolites are derived from a normal crystallization sequence at depth (magnetite, ilmenite, apatite, zircon, sphene, pyroxene, plagioclase, amphibole, alkali feldspar, feldspathoid) that was superimposed by reverse paragenesis (feldspathoid, alkali feldspar, Zr/Ti silicates, alkali pyroxene) developed at lower depth. The role of CO_2 transfers during the development of these phonolites has been proposed by Batard and al. (1977). Mergoil (1968) has pointed out an intense transfer of CO_2-rich fluids that affected the phonolite of the Suc de Sara along its eastern margin including the surrounding metamorphic basement during its final emplacement. The possible origin of theses volatile-rich melts is discussed by Martin et al. (2017).

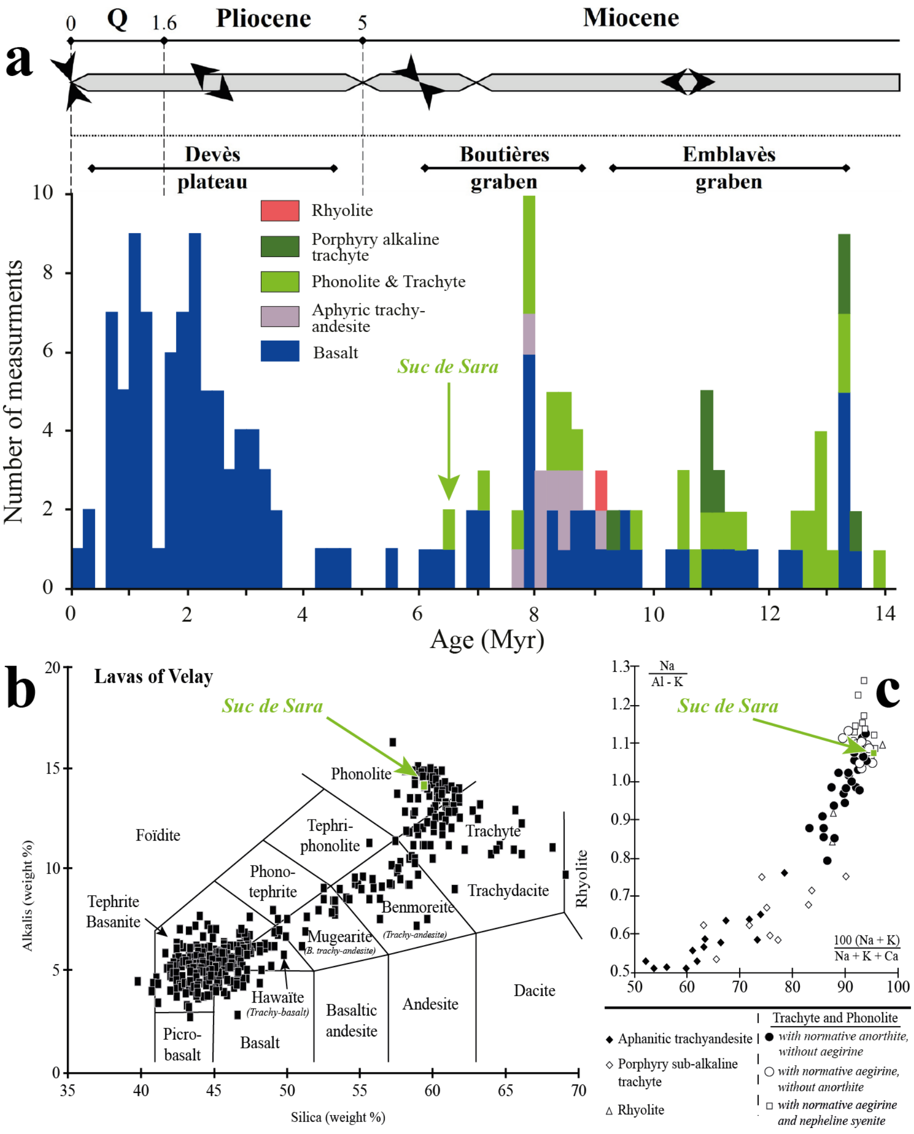

Figure 2. **(a)** Histogram summarizing the number of geochronological ages of volcanic edifices in the Velay massif according to their composition (modified from Mergoil and Boivin, 1993) and direction of the main constraints represented by the black arrows (modified from Blès et al., 1989). The 6.5 Myr old Suc de Sara represents the youngest phonolitic edifice. **(b)** Total alkali silica (TAS) diagram (Le Bas et al., 1986) of the Velay alkaline series (modified from Mergoil and Boivin, 1993). **(c)** Peralkalinity diagram for differentiated products from the Velay province (modified from Mergoil and Boivin, 1993).

2.3 The Suc de Sara intrusion

The Suc de Sara intrusion has been the subject of studies since the 1970s (Mergoil, 1968). This vertical arched structure is located in the “Cirque des Boutières” and culminates at 1521 m (Figs. 1, 3a, b; Saint Martin, 2009). It has been interpreted so far as a ring dyke structure shallow-emplaced in a late Miocene graben free of sedimentation affecting a Variscan basement composed of gneiss and metatexite (Mergoil and Boivin, 1993, and references therein). This intrusion is a phonolite with a thickness varying between 50 and 390 m (Fig. 3a). It is defined by $\mathrm{Na+K/Al} > 1$ (Mergoil, 1968). According to Mergoil (1968), its alkaline chemical composition grants a mineralogy enriched in sodium and potassium with the presence of sodic pyroxenes (aegirine–augite), aenigmatite, and alkali feldspars (sanidine, orthoclase, or microcline). Moreover, the rock contains a large proportion of feldspathoids (nepheline and sodalite), testifying to its undersaturation in $\mathrm{SiO_2}$ (Mergoil, 1968).

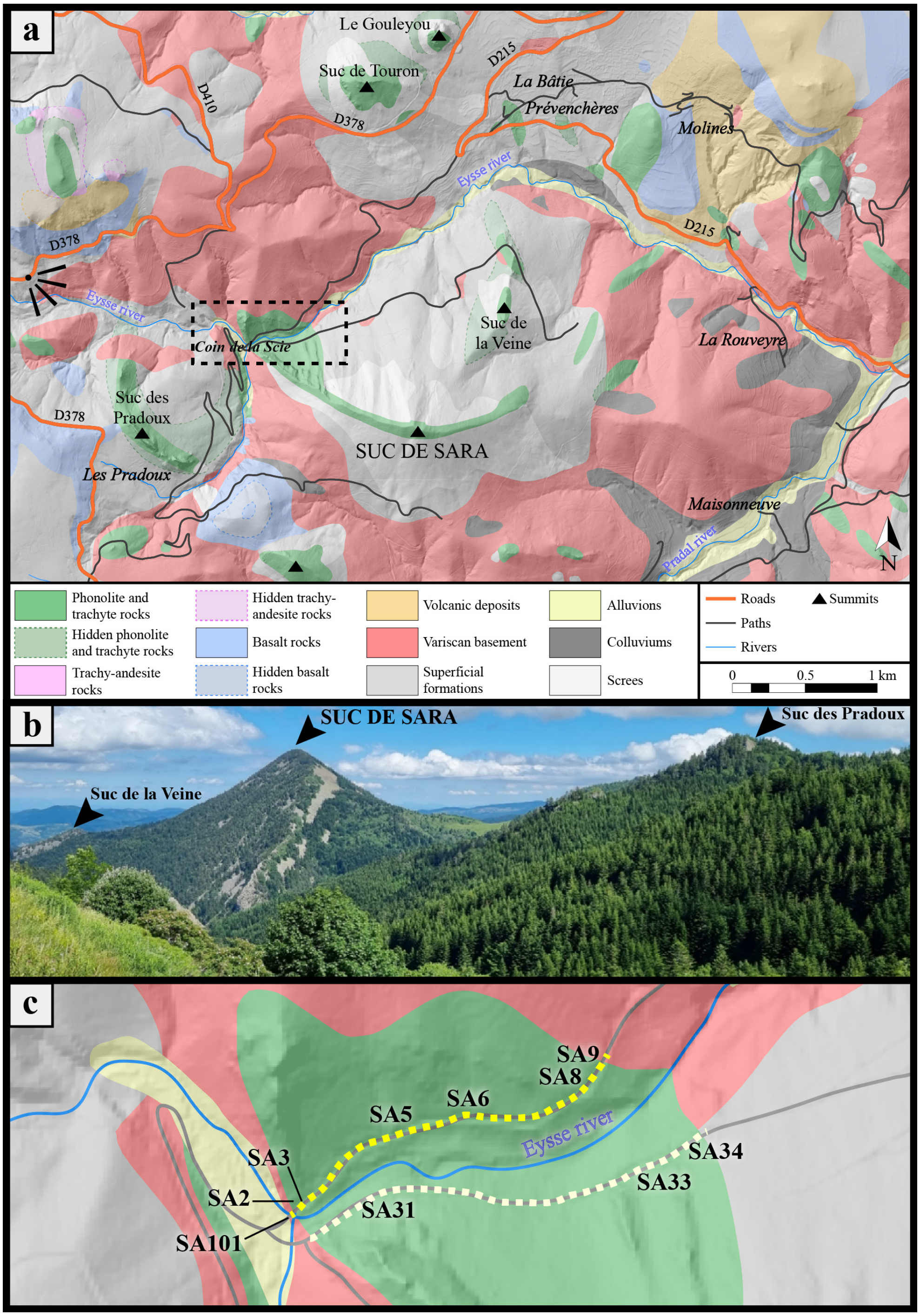

Figure 3. **(a)** Simplified geological map of the Suc de Sara area ("Cirque des Boutières" graben; see location in Fig. 1b. Modified from BRGM (2011) 1 : 50 000 geological map no. 816, Le Monastier-sur-Gazeille, Defive et al., 2011). Digital terrain model generated from data supplied by Institut Géographique National, https://geoservices.ign.fr/rgealti (last access: 24 January 2022). The pictogram corresponds to the panoramic view of **(b)**. The red insert corresponds to **(c)**. **(b)** Panoramic view of the "Cirque des Boutières" with three visible summits: the Suc de la Veine, the Suc de Sara, and the Suc des Pradoux. **(c)** Close-up view from **(a)** on the western part of the intrusion which represents the two sections on either side of the river Eysse where we carried out our observations and sampling. Each sample code name is listed in Table 1. The yellow dotted line corresponds to the section presented in Fig. 7.

3 Analytical methods

3.1 Linear analysis with Hough transform

We analysed the regional-scale spatial distribution and determined the best alignment directions of the 505 monogenetic vents identified in the area of 1800 km^2 of the eastern Velay (Mergoil and Boivin, 1993). We used three 1 : 50 000 geological maps: Le Puy (number, 791; Girod et al., 1979), Le Monastier-sur-Gazeille (number 816; Defive et al., 2011), and Burzet (number 840; Bambier et al., 1985). We applied the Hough transform method, which is a pattern recognition technique used in digital image processing. The principle of this method is based on the detection of potential alignments in an image, despite imperfections such as noise (Hough, 1959). The technique consists of placing objects of interest in a Cartesian space (x, y) and transforming them into curves in the Hough space according to a distance and an angle (ρ, θ). The formula linking both is as follows:

$$(D) : \rho = x \cdot \cos(\theta) + y \cdot \sin(\theta). \quad (1)$$

In the Hough space, the Cartesian equation of a line (D) is expressed by polar coordinates with ρ the distance of the line from the origin of the reference frame and θ (between 0 and 360°) the angle that the perpendicular to the line makes with the x axis. Each point identified in the Cartesian space will allow a projection in the plane of the polar coordinates of all the lines that pass through this point (Hart and Duda, 1972). An example of the calculation performed with the software coded in the Python language is presented in Fig. A1 in the Appendix.

3.2 Structural and textural cross-section

An east–west detailed cross-section along the Eysse valley, including textural observations, structural measurements, and sampling, was made along the thicker northwestern part of the Suc de Sara dyke till the surrounding metatexites (Fig. 3c). Structural measurements included fracture population analyses in the basement and foliation, vein, and mineral banding measurements in the dyke. A total of 10 phonolite samples were selected as representative of the different facies observed in the field (Fig. 3c). The criteria were local enrichment in alkali feldspar and nepheline phenocrysts and the transition from medium-grained phaneritic to aphanitic and porphyritic textures, the latter being locally cut by aegirine veins and localized shear bands.

3.3 Textural and chemical analyses

The samples selected for petrography, scanning electron microscopy (SEM) textural characterization, mineral chemistry, and bulk rock composition are listed in Table 1. Samples selected for microstructural and petrographic analyses were cut following a section parallel to the mineral lineation and perpendicular to the foliation ($[x, z]$ structural plane with x the mineral lineation and z the normal of the foliation plane). The resulting thin sections were first observed under a polarizing optical microscope in order to characterize all the different textures and the associated mineral paragenesis recognized in the Suc de Sara intrusion. Subsequent analyses included backscattered high-resolution image acquisition using a scanning electron microscope (Merlin Compact Zeiss hosted in the Institut des Sciences de la Terre d'Orléans – ISTO) with an acceleration voltage of 15 kV and a working distance of 10 mm. In addition, semi-quantitative chemical mapping was performed by using a Bruker QUANTAX XFlash6 wavelength-dispersive spectroscope (WDS) available on the SEM. Quantitative chemical mineral analyses and mapping were performed using two electron microprobes (EPMA; Cameca SX Five and JEOL iHP200F, both equipped with five WDS spectrometers and hosted in ISTO) with an acceleration voltage of 15 kV and a beam current of 10 nA. Counting time for each element was 10 s per peak for punctual analysis; a dwell time of 100 ms was used for chemical maps. The detection limits are of the order of 900 ppm for Si and K; of 400 ppm for Al, Na, and Ca; and of less than 2000 ppm for Fe and Ti.

3.4 Whole-rock analysis

Major elements were analysed by inductively coupled plasma optical emission spectroscopy (ICP-OES) at Laboratoire Magmas et Volcans (LMV, Clermont-Ferrand, France). Powdered samples were melted with $LiBO_2$ in a magnetic induction oven at 1100 °C for 5 min using graphite crucibles. The glass beads were then dissolved in a solution of deionized water and nitric acid (1 M) and diluted by a factor of 2000 to produce the solution to be analysed by an Agilent 5800 VDV ICP-OES in radial mode. Analytical uncertainties ($\pm 2\sigma$) vary between 1 % and 3 % except for K_2O, MnO (4 %), and P_2O_5 (7 %) for the DR-N standard (diorite). The conditions of analysis are as follows: plasma flow 12 L min^{-1}, nebulizer flow 0.7 L min^{-1}, and RF power 1.2 kW.

3.5 Raman spectroscopy

The structural and chemical identification of late-magmatic phases was performed using Raman spectroscopy. The spectra were recorded using a micro-Raman apparatus hosted in ISTO and equipped with a monochromatic 532 nm Coherent Genesis MX SLM laser as excitation source, a Nikon ECLIPSE Ni–U microscope, an Andor Shamrock 500i spectrometer, and Peltier cooled back-illuminated CCD Andor Newton detector. The use of a long-working-distance Nikon objective (100×, N.A. 0.8) allowed micro-scale analysis with lateral resolution down to 1–2 μm^2. The 1200 lines mm^{-1} grating was employed to record two spectral windows of interest: the main silicate network spanning from 100 to 1400 cm^{-1} and the OH stretching region from to 2800 to

Table 1. List of samples used in this study with their geographical coordinates and the type of analysis performed on each sample.

	Coordinates		Analysis			
Sample SA-	*x*	*y*	Petrography	SEM textural analysis	EPMA phase analysis	Bulk rock chemistry
2	44.877860	4.207730	●			
3	44.877860	4.207730	●	●	●	●
5	44.878530	4.209210	●			
6	44.878710	4.210400	●	●	●	●
8	44.878770	4.211650	●			
9	44.878920	4.211970	●	●	●	
31	45.079335	4.093647				●
33	45.079335	4.093647				●
34	44.878432	4.213421				●
101	44.877860	4.207730				●

3800 cm^{-1}. Each spectrum was recorded during 60 s (two acquisitions of 30 s) under the laser power output of 200 mW. Daily calibration of the Raman micro-spectrometer was performed based on the main 520 cm^{-1} peak of silicon.

4 Results

4.1 Lineament analysis

A simplified map that includes the 505 vents identified on geological maps to be analysed with the Hough transform analysis is shown in Fig. A2.

First, we applied the Hough transform to all 505 vents (Fig. 4). For this first case, one node stands out clearly at N146° E (symmetrically, the same node stands at N326°), but more discreet directions not calculated can be recognized such as the N010° E and N110° E directions (Fig. 4a, b). In a second analysis, we discriminated the mafic and felsic vents (Fig. 4c, d, e, f). The Hough transform analysis on mafic vents show four main alignments – N011° E, N103° E, N112° E, and N140° E – while the felsic vents show only two major directions: N110° E and N142° E.

Complementary field measurements on fracture networks affecting the Variscan gneisses in several locations near the Suc de Sara intrusion and in the phonolite itself were performed (Fig. 5). Analyses confirm the existence of two main associated populations of brittle structures mostly oriented N080° E–N090° E and N140° E affecting the basement. In addition, a third minor direction represented by N050° E fractures is identified (Fig. 5a). Measurements within the Suc de Sara allow us to follow the foliation direction of this intrusion from the “Coin de la Scie” to the summit (Fig. 5b). It can be seen that the main foliation plane rotates between the northwest end and the summit of the Suc de Sara.

4.2 Fracture network analyses

We conducted a regional, joint, and shear fracture analysis based on 16 sites: 9 sites distributed in the country rock and 7 sites located in the intrusion (Fig. 5). Low-dipping fractures, i.e. fractures dipping less than about 10°, were not measured as they generally can be either exfoliation or unloading joints.

In the Velay basement two main fracture populations are recognized (Fig. 5a). N120° E–N140° E striking fractures are associated with N010° E–N020° E striking fractures, all being highly dipping. These two fracture sets are observed in the far field (stereographic diagrams 3, 8, and 9 in Fig. 5a) but also in the vicinity of the Suc de Sara intrusion (stereographic diagram 1 in Fig. 5a). A third fracture population composed of almost east–west-striking fractures is also observed (stereographic diagrams 4, 5, 6, and 7 in Fig. 5a). This population consists of two associated sets of fractures moderately dipping (from 20 to 45°) either to the north or to the south.

In the Suc de Sara intrusion, three populations of fractures are observed (Fig. 5b). The orientation and dip of these fractures evolve with respect to their location in the intrusion. The main population is composed of fractures parallel to the closet hanging wall of the intrusion, while the two associated populations exhibit nearly perpendicular striking directions. The first population corresponds to fractures parallel to the local mineral foliation (see measurements hereafter), while the two other populations are identified as prismatic joints. The associated N120° E–N140° E and N10° E–N20° E striking fractures recognized in the country rock are not developed in the intrusion, meaning that they were not any more active during and after the emplacement of the intrusion.

4.3 Mineral fabrics

Mineral foliations and lineations were measured within the Suc de Sara intrusion by using the shape preferred orientation of elongated pyroxene, as well as alkali feldspar porphyroclasts, when present. Mineral lineation is usually hardly distinguishable in the field; only five lineations were measured in the eastern area. Their orientations range from N0° E to N030° E and from N110° E to N170° E. The associated dips

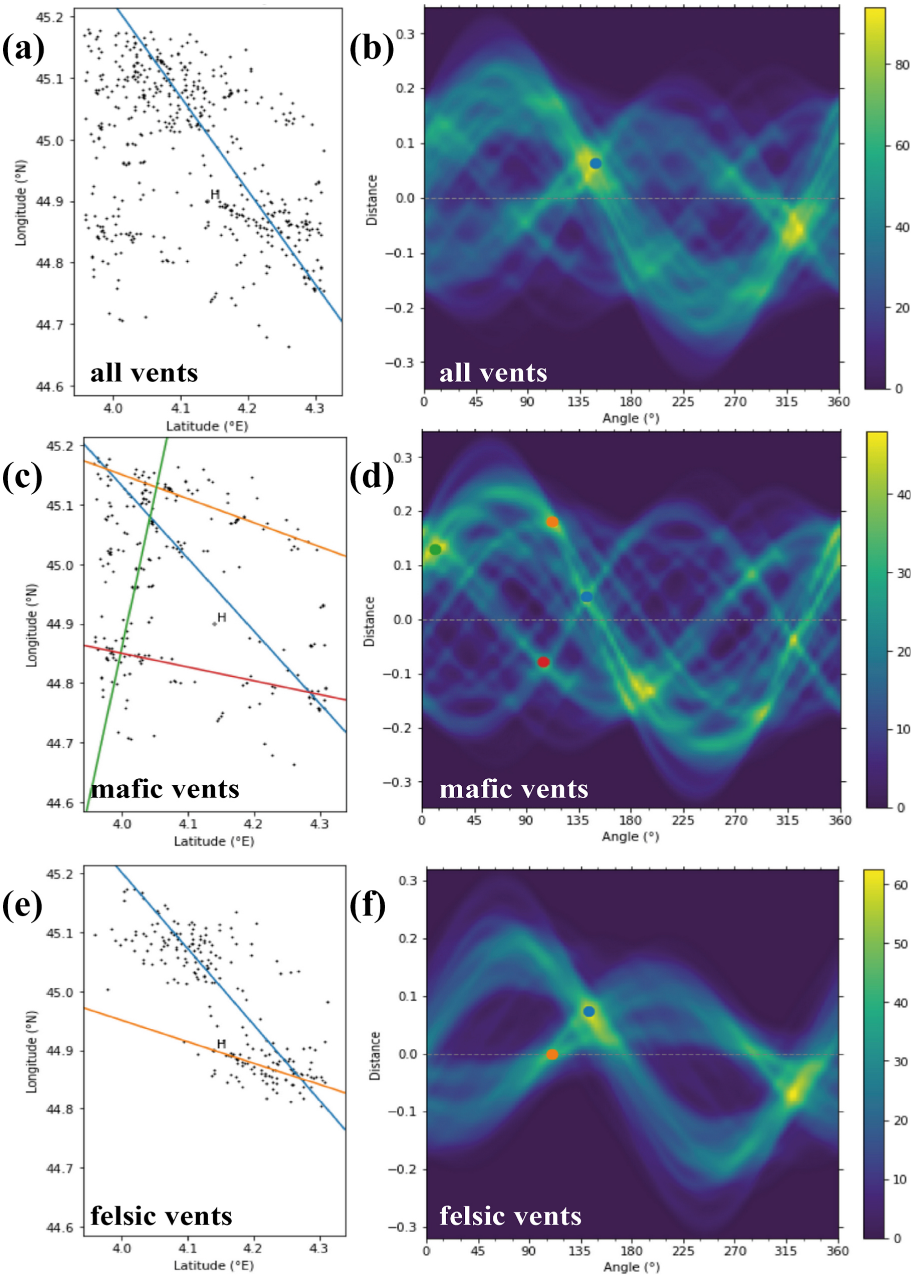

Figure 4. Hough transform applied to monogenic vents of the eastern Velay **(a, b)**, only to mafic vents **(c, d)**, and only to felsic vents **(e, f)**. The diagrams on the left **(a, c, e)** correspond to Cartesian spaces. The H points correspond to the Hough centre from which the distance ρ is calculated. The points on the right diagrams represent the main nodes, and their associated line is drawn on the Cartesian space. The blue to yellow gauges represent the number of curves that overlap in Hough space.

range from 30 to 45°, with an almost horizontal dip measured at the heart of the structure (Fig. 6).

In the vicinity of the intrusion margin, the mineral foliation always trends parallel to the margin. They dip between 35 and 75° along the northwest margin, but they are more generally dipping at 80° on average. In the core of the structure, the foliation progressively evolves to a 20° dip to the north (Fig. 6). The inferred foliations trajectories based on our measurements express an axial structure.

4.4 Cross-section

The detailed cross-section that lies perpendicularly to the margins of the intrusion was performed by combining ob-

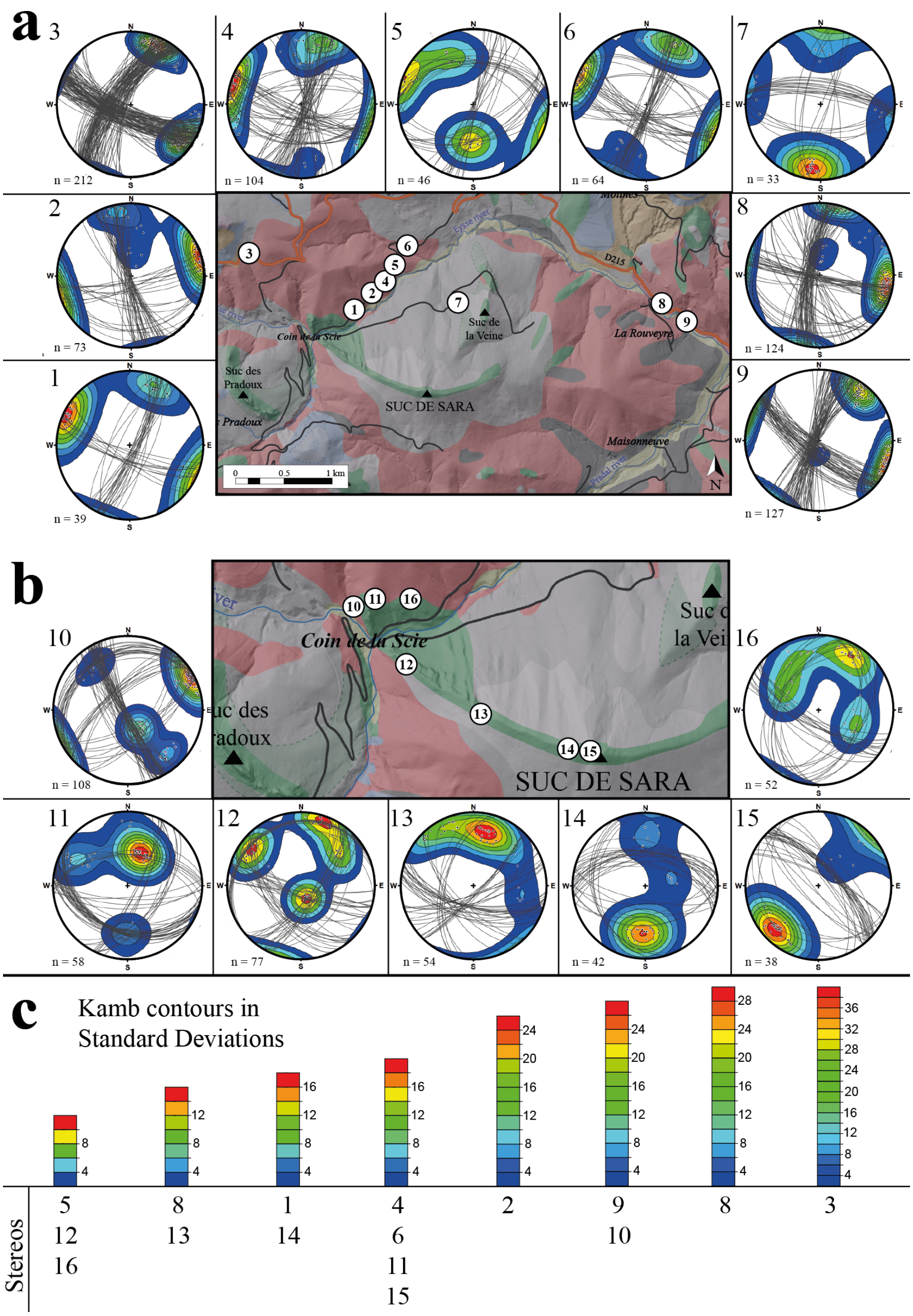

Figure 5. **(a)** Fragile tectonic history of the late-Variscan basement around the Suc de Sara since 295 Ma (Cirque des Boutières). **(b)** Fracturing recorded since 6.5 Ma by the Suc de Sara with anisotropy linked to foliation. **(c)** Statistical densities of the pole population contoured at intervals of standard deviation following the Kamb contour method. Equal-area stereographic projections, lower hemisphere. The map legend as in Fig. 3. Geological maps modified from 1 : 50 000 geological map no. 816, Le Monastier-sur-Gazeille, Defive et al. (2011).

servations along the two pathways on both sides of the Eysse river and in the riverbed (Fig. 7a).

On the western margin of the intrusion, the surrounding Variscan metamorphic basement formed of biotite-rich metatexites outcrops in the riverbed. The margins of the dyke trend N140° E and dip 76° to the west (Fig. 6). It is composed of a 10 to 15 cm thick glassy phonolite in which rare alkali feldspar phenocrysts are present. The inner zone is constituted by an aphanitic and porphyritic phonolite whose mineral foliation is parallel to the margin of the dyke (Fig. 7a and b). Rare alkali feldspar phenocrysts show a rounded shape (Fig. 8a, b). These two facies are crosscut by two set of veins filled by aegirine (Fig. 8a). The first set is composed of long and locally thick veins parallel to the main foliation. They

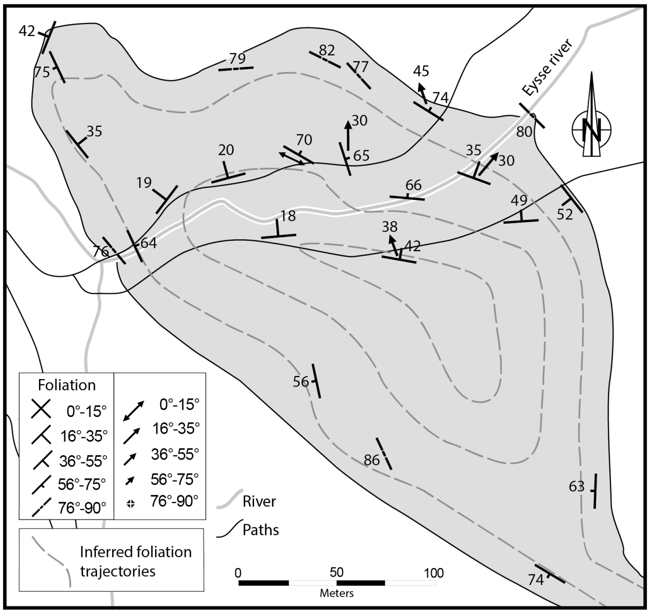

Figure 6. Mineral foliations and lineations measured in the northwestern extension of the Suc de Sara intrusion. Inferred trajectories exemplify the axisymmetric nature of the thicker northwestern part of the intrusion.

are connected to a second set of veins, both forming an anastomosed pattern (Fig. 8a). From place to place, and in particular close to the glassy margin, this second set becomes predominant. The orientation of the shear planes C (parallel to the foliation planes S) and the associated planes C′ marked by certain aegirine veins and further from the glassy margin by aegirine crystals is schematized in Fig. 9. From the margin and about 2 m to the east, the texture changes as the rock exhibits progressively a phaneritic texture (tinguaite facies) with infra-centimetric feldspar, idiomorphic nepheline, and elongated aegirine; the orientation of the latter defines a clear foliation parallel to the margin of the dyke. Scattered fractures are still present but are progressively replaced when moving away from the margin by a dense network of veins parallel to the main mineral foliation and composed of aligned aegirine grains (Fig. 8b, c).

Approaching the centre of the intrusion the tinguaite becomes rich in alkali feldspar phenocrysts, while aegirine-rich veins are no longer present (Fig. 8d). Aegirine phenocrysts define an S-type fabric as the well-marked foliation does not include any lineation (Fig. 8d). At the same location the N75°oriented bending discrete foliation rapidly bent to become almost horizontal before becoming a 65° bending to the east 100 m eastward (Fig. 7a). The intrusion is crosscut by two N145° E and N016° E trending brittle faults (Fig. 7).

Along the eastern margin the tinguaite is crosscut by rare, aegirine-rich veins without a preferred orientation observed. In addition, the tinguaite exhibits a horizontal columnar jointing (Figs. 7a, 8e) indicating that no shearing affected the tinguaite during the late cooling magmatic stage. The eastern margin between the intrusion and the country rock well crops out in the Eysse riverbed, and it is characterized by the presence of a 1 m thick composite polygenic breccia consisting of phonolitic and gneissic blocks embedded in a porous, coarse-grained matrix (Figs. A3, A4). Close to this breccia, a basaltic dyke, barely parallel to the margin of the intrusion, intrudes the tinguaite as it was already fully crystallized (Fig. A3). The metatexite forming the country rock is strongly altered over about 15 m from the contact margin. This metasomatic alteration that involves the removal of the silica corresponding to the so-called fenitization is caused by the circulation of magmatic fluids under pressure from the intrusion into the surrounding rock (Mergoil, 1968). This alkaline alteration is expressed by the disappearance of the biotite and a strong dequartzification; this latter process left spaces that are locally filled by aegirine as geodic crystallizations, while veins of similar origin to those affecting the phonolite are also present (Figs. 8f, A4).

4.5 Whole-rock geochemistry

The whole-rock analyses of six representative samples are presented in Table 2. The locations of samples SA3, SA31, SA6, SA33, SA34, and SA101 are shown in Fig. 3c.

For all whole-rock analyses of the Suc de Sara intrusion point in the phonolite domain (Fig. 2b), SiO_2 (60.08 ± 0.12) and $Na_2O + K_2O$ (14.78 ± 0.28) contents confirm the general SiO_2 undersaturation of the Suc de Sara intrusion. Among the analysed oxides, only Na_2O shows a significant variation from the margin to the core of the intrusion (Fig. 10a). In particular, the western margin of the structure represented by sample SA3 is the most alkali-rich, in agreement with the large amount of idiomorphic nepheline phenocrysts. In the peralkalinity diagram, the Na / Al–K ratio values range from 1.04 for SA33 to 1.20 for SA101 (Fig. 10b).

4.6 Microscopic analysis

To unravel the mineral associations and textures present in the different facies of the Suc de Sara intrusion, we selected six $[x, z]$ oriented thin sections representative of the main textures recognized in the field (Table 1). In order to simplify the description, they are grouped in three main zones, namely the western margin (SA2 and SA3), the core of the intrusion (SA5 and SA6), and the eastern margin (SA8 and SA9). The glassy zone that marks the western contact with the basement is not taken in consideration.

4.6.1 Petrography

The different facies of the margins and the core facies of the Suc de Sara intrusion were observed under a polarizing optical microscope (Fig. 11). At the western margin, the phono-

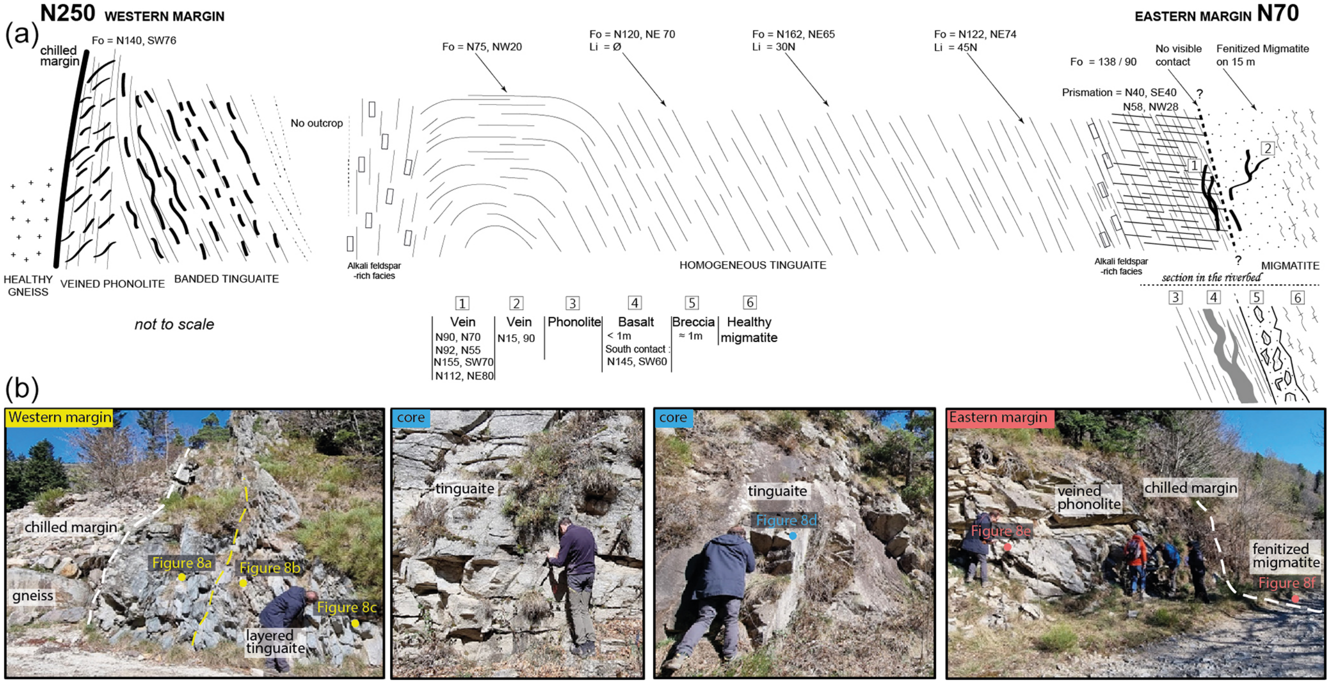

Figure 7. **(a)** Detailed cross-section of the Suc de Sara phonolitic intrusion at the level of the path above the Eysse River, based on the outcrops on the left and right banks. The location of the section is available in Fig. 3. **(b)** Photos of outcrops on the north bank. Fo signifies mineral foliation, Li signifies mineral lineation, and P signifies fault plane with L signifying striae.

Table 2. Whole-rock analyses of the Suc de Sara. Analysis of Mergoil and Boivin (1993) performed on a sample taken in the core along the same section is given for comparison (n.d.: no data).

	This study						Mergoil and Boivin (1993)
Sample name Location	SA101 Western margin	SA3 Western margin	SA31 Core	SA6 Core	SA33 Eastern margin	SA34 Eastern margin	73–79 Core
SiO_2	59.60	60.34	60.11	60.12	60.27	60.05	59.52
Al_2O_3	19.99	20.27	20.08	20.16	20.04	20.11	20.05
Fe_2O_3	2.84	3.09	2.95	3.06	2.89	2.98	3.34
MgO	0.03	0.09	0.04	0.02	0.03	0.02	n.d.
CaO	0.66	0.75	0.72	0.77	0.70	0.68	0.66
Na_2O	10.36	10.04	9.48	9.45	9.23	9.47	9.11
K_2O	5.22	5.05	5.14	5.09	5.10	5.05	4.97
TiO_2	0.15	0.16	0.16	0.16	0.16	0.16	0.23
MnO	0.25	0.29	0.28	0.29	0.28	0.29	0.28
Ba	0.0005	0.0015	0.0013	0.0009	0.0013	0.0008	n.d.
Sr	0.0001	0.0004	0.0007	0.0004	0.0007	0.0004	n.d.
H_2O+	0.04	0.25	0.34	0.26	0.36	0.29	n.d.
H_2O-	0.062	1.11	2.01	1.52	2.00	1.71	n.d.
Total	101.30	101.42	101.30	100.89	101.05	100.80	98.18

lite exhibits an aphanitic, feldspathoids-rich (nepheline and sodalite) porphyritic and trachytic texture formed by rare alkali feldspar phenocrysts embedded in a groundmass composed of aligned alkali feldspar and aegirine microlites. The rod-like habit of some aegirines suggests a rapid crystallization consistent with the frozen wall facies.

The core facies is represented by the tinguaite (Fig. 11c, d). Its paragenesis is broadly similar to those observed in the phonolite of the margin with sparse phenocrysts of al-

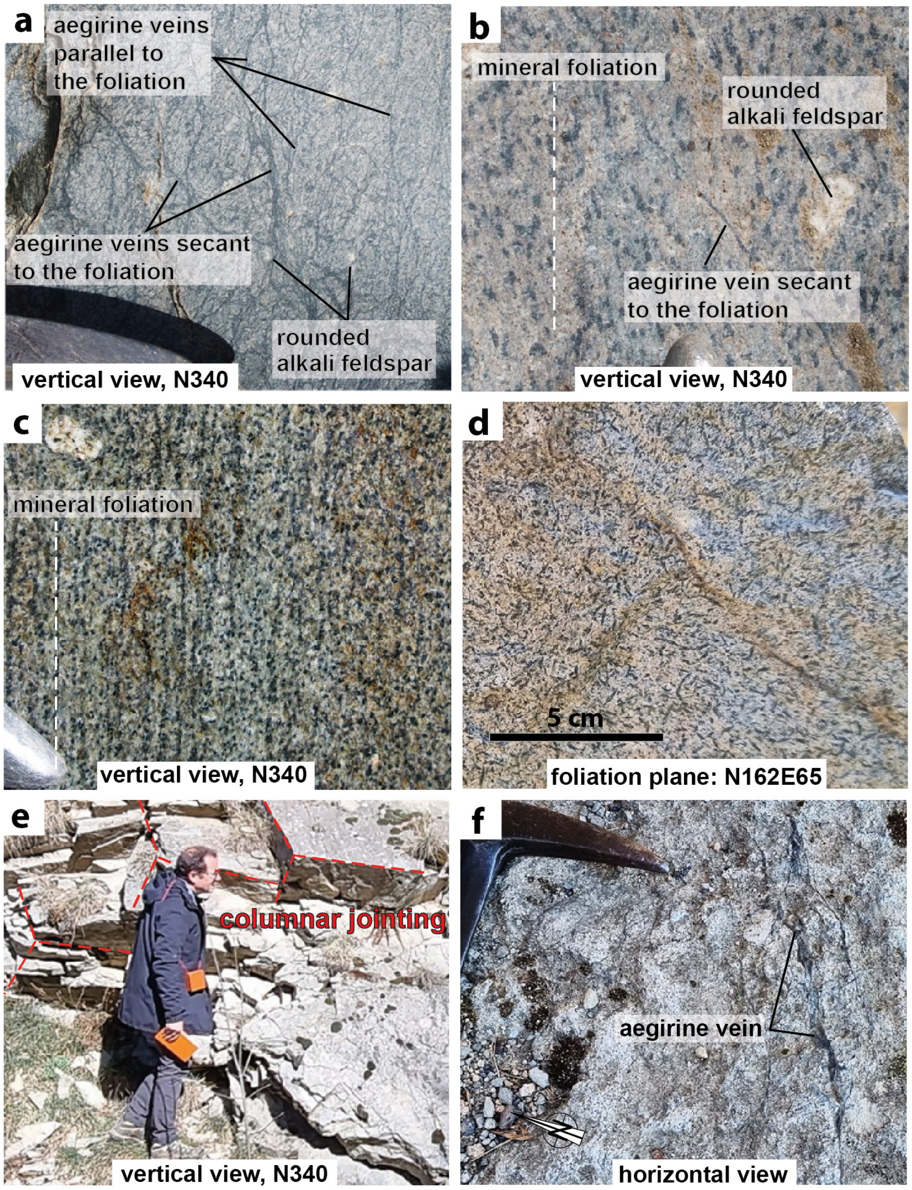

Figure 8. Field photographs detailing the main structures observed across the intrusion. The position of each figure is shown in Fig. 7. **(a)** Aegirine-bearing vein network and alkali feldspar phenocrysts observed on the western margin. **(b)** Aegirine-bearing veins crosscut the mineral foliation that wraps around an alkali feldspar phenocryst. **(c)** Aegirine banding and alkali feldspar phenocrysts observed in the tinguaite away from the western margin. **(d)** Idiomorphic aegirine and alkali feldspar phenocrysts exhibiting a weak shape fabric orientation observed in the core of the structure. **(e)** Sub-horizontal columnar jointing of the phonolite observed near its eastern margin. **(f)** Aegirine-bearing veins observed in the fenitized migmatitic host rock at about 1 m from the eastern margin.

kali feldspars and albites. However, feldspars are in lower proportion at 130 m from the western margin (Fig. 11c). But they are again more present further away (Fig. 11d) to the east where aegirines are in lower abundance and most often interstitial. Moving to the east, the phaneritic texture changes as it becomes progressively aphanitic and porphyritic approaching the eastern margin (SA7; Fig. 11e, f). Nepheline is present as microlites together with alkali feldspar and albite in the groundmass (Fig. 11f).

4.6.2 SEM textural analysis

Scanning electron microscopy (SEM) analyses were done on the three main facies by combining backscattered electron (BSE) images (Fig. 12) and compositional mapping using wavelength-dispersive X-ray spectroscopy (WDS; Figs. A5, A6).

In the thin section SA3 representative of the western margin, idiomorphic alkali feldspar phenocrysts exhibit

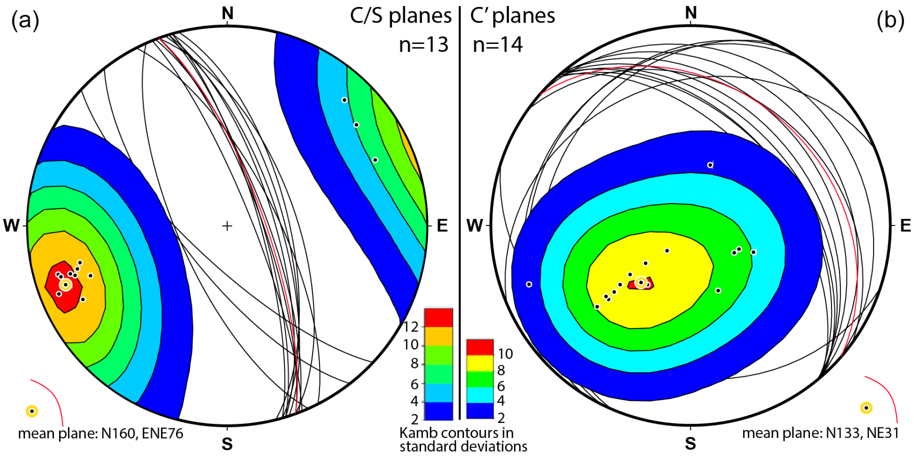

Figure 9. Stereographic diagrams (Schmidt equal-area projection, lower hemisphere) of associated C (**a**, parallel to the mineral foliation S) and C′ (**b**) aegirine-bearing shear bands measured near the chilled western margin (SA3 location in Fig. 7 and picture in Fig. 8a). Statistical densities of the pole population contoured at intervals of standard deviation following the Kamb contour method.

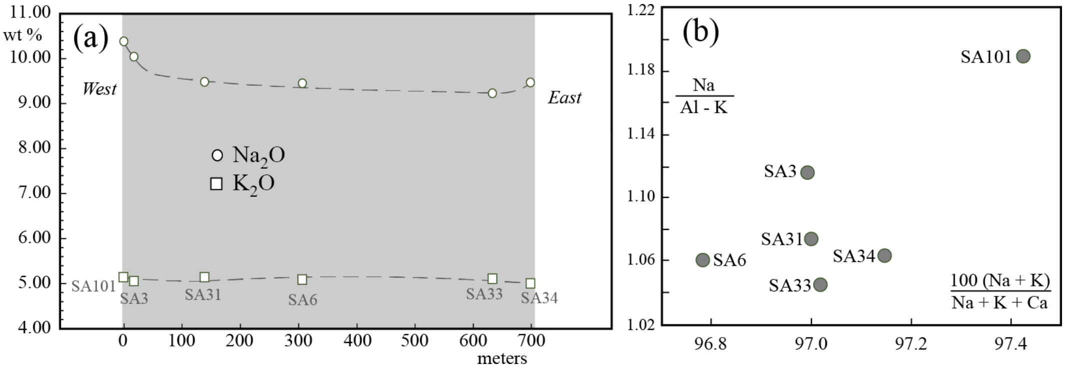

Figure 10. (**a**) Variation in Na_2O and K_2O along the cross-section. (**b**) Position of representative samples in the peralkalinity diagram.

potassium-rich overgrowths (Figs. 12a, A5, A6). In addition, they are affected by late albite recrystallization mainly developed on the periphery of phenocrysts but also locally propagated into the phenocryst by following the crystallographic planes (Fig. 12b). The phenocrysts are embedded in a groundmass composed of feldspathoids (nepheline and sodalite), sodic pyroxene (aegirine), aenigmatite, alkali feldspar, and albite. Pyroxenes are idiomorphic and exhibit a poikilitic texture as they have included the smallest idiomorphic feldspar microlites. At larger scale not shown in Fig. 12, these pyroxenes locally form ribbons, as observed on a macroscopic scale in the field (Fig. 8c). Aenigmatites are also often idiomorphic and usually associated with pyroxenes. As also observed with feldspar phenocrysts, square sections of nepheline grains exhibit a reaction rim of albite composition (Fig. 12b). Finally, the matrix shows a limited porosity expressed as isolated pores entrapped between feldspar microlites (Fig. 12a).

In the central part of the intrusion, where the foliation is nearly horizontal, the tinguaite contains a larger population of phenocrysts with a centimetric size (SA5; Fig. 11c). The coarser grains are alkali feldspar, some of them with a sanidine composition. Many of these large phenocrysts are intensively recrystallized with the development of large domains of albitic composition associated with an extensive porosity (Fig. 12c). Nepheline is still present but as rounded grains with a maximum diameter of 50 µm (Fig. 12d). Aenigmatite is absent. The groundmass exhibits a strong shape fabric marked by the alignment of the feldspar microlites wrapping around the phenocrysts. Other microlites are rounded albite grains and, punctually, idiomorphic oxides (titanomagnetite) smaller than 50 µm. Locally in this groundmass, millimetric poikilitic crystals of aegirine are present (Fig. 12d). The alkali feldspar embedded in these poikilitic aegirine exhibits rounded shape, implying re-equilibration processes with the pyroxene (Fig. 12d). The porosity is also present in abundance in the groundmass.

Close to the eastern margin (SA8 and SA9) the paragenesis is similar to the one observed on the western side (Fig. 12a, b, e, f). Both idiomorphic alkali feldspar phenocrysts and nepheline microlites exhibit albitic rim overgrowth (Fig. 12e). In the feldspar-rich groundmass, aegirine

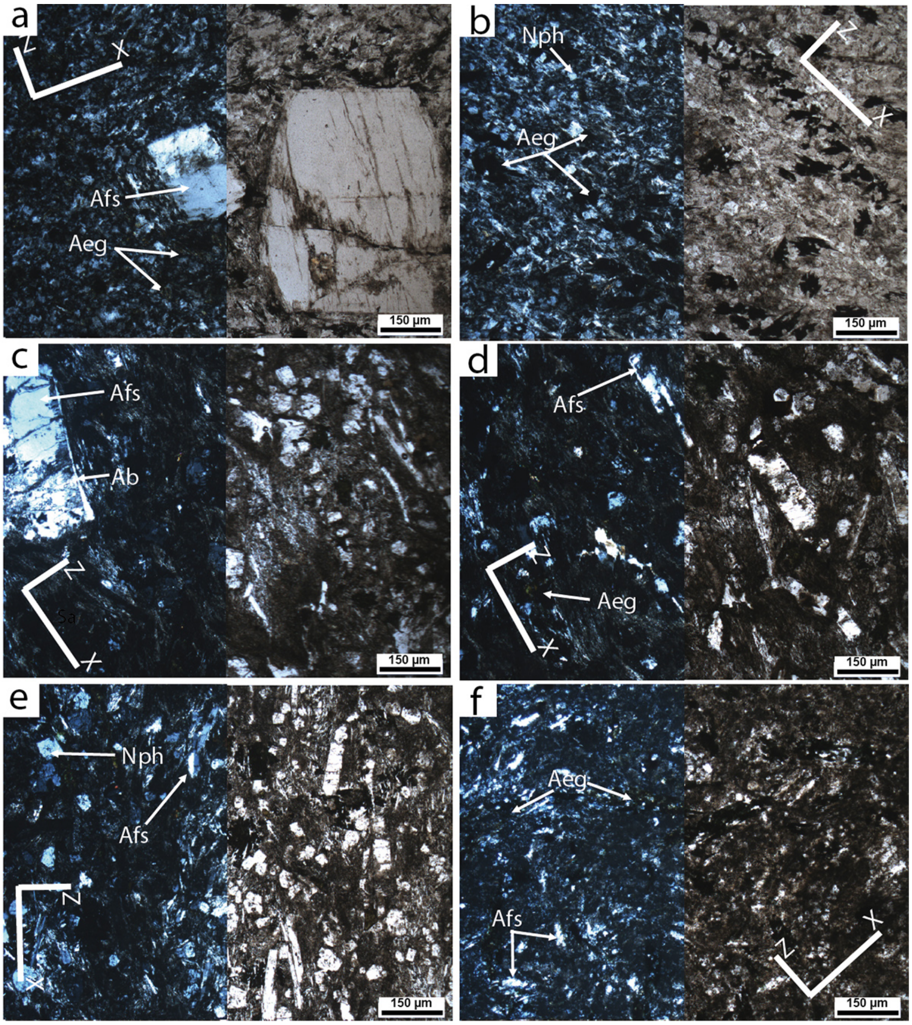

Figure 11. Characteristic textures observed in the Suc de Sara intrusion. All images are $[x, z]$ sections (with x as the lineation) and divided in cross-polarized light half image (left) and in plane-polarized light half image (right). The position of the samples is shown in Fig. 3c. Panels **(a)** and **(b)** represent trachytic textures of the western margin. Panel **(a)** is the veined phonolite (SA101, corresponding to the field view of Fig. 8a) characterized by idiomorphic pristine alkali feldspar with albite corona embedded in an aegirine (Aeg)-rich aphanitic groundmass. Panel **(b)** is the banded phonolite (SA2, corresponding to the picture of Fig. 8c) characterized by the alignment of 100 µm long poikilitic aegirine (upper-left corner). Panels **(c)** and **(d)** represent the texture of the tinguaite forming the core area (SA5 in Fig. 8d). Note the abundance of aligned prismatic alkali feldspar phenocrysts showing Carlsbad twinning, all being intensively altered. They are just a little less present at the apex of the intrusion. Panels **(e)** and **(f)** represent the transition from tinguaite texture (**e**, SA7) and the phonolite texture (**f**, SA9) approaching the eastern margin. The pristine alkali feldspars mark the lineation in the nepheline-rich tinguaite. In both facies the aegirine is present as poikilitic, 100–200 µm long crystals in the groundmass. The mineral abbreviations are derived from Warr (2021): Ab signifies albite, Aeg signifies aegirine, Afs signifies alkali feldspar, and Nph signifies nepheline.

remains abundant, still with a poikilitic texture as it encompasses both square-shaped albite grains and alkali feldspar microlites.

4.6.3 Mineral chemistry

The chemical data are presented in the Appendix. For iron-containing minerals, we used the Droop (1987) method to separate Fe^{2+} and Fe^{3+} from the total FeO content.

Alkali feldspar

Alkali feldspar is the most abundant phase and spread over a wide compositional range in the ternary diagram between the potassium and sodium poles (Fig. 13a; Tables A1 and A2 in the Appendix). The core of the feldspar phenocrysts found in the three facies is potassic anorthoclase to sanidine in composition in the range $Ab_{68–44}Or_{32–56}An_{0–4}$. All phenocrysts exhibit a margin of sodic anorthoclase to albite compositionally in the range $Ab_{98–80}Or_{2–20}An_{0–9}$. The albitic com-

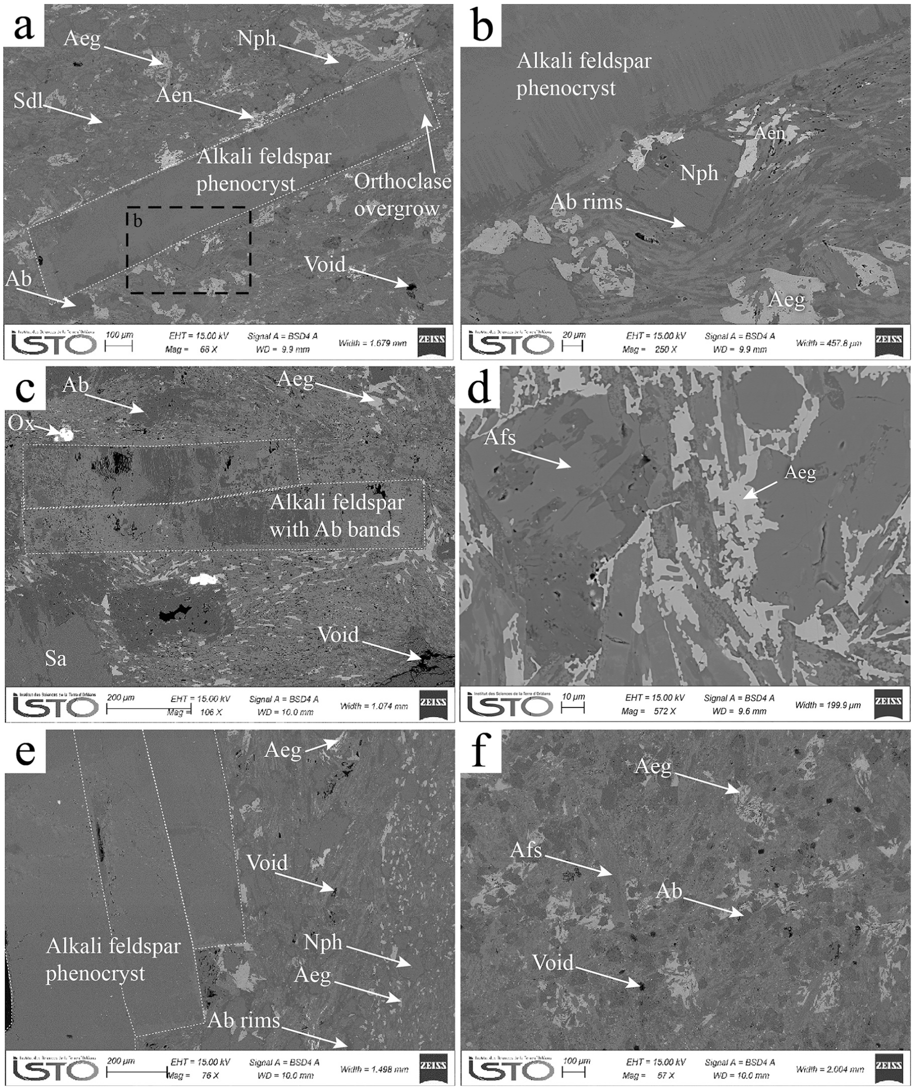

Figure 12. Backscattered electron (BSE) photography. **(a)** Section SA3 (western margin). The dotted rectangle represents the enlargement in **(b)**. **(b)** Zoom from Fig. 12a showing the albitic rims developed around alkali feldspars and nepheline phenocrysts. **(c)** Section SA5 (core). **(d)** Close-up view from section SA6 (core). Note the partially resorbed alkali feldspar microliths in contact with the interstitial aegirine. **(e)** Section SA8 (eastern margin). **(f)** Section SA9 (eastern margin). The mineral abbreviations are derived from Warr (2021): Ab signifies albite, Aen signifies aenigmatite, Aeg signifies aegirine, Afs signifies alkali feldspar, Nph signifies nepheline, Ox signifies oxide, Sa signifies sanidine, and Sdl signifies sodalite.

position constitutes the irregularly developed most external rim in contact with the groundmass (Fig. A5, A6). Finally, potassium-dominated sanidine to nearly pure orthoclase ($Ab_{2–18}Or_{81–98}An_{0–6}$; Fig. 13a) overgrowth occurs, particularly in phonolite from the western margin of the intrusion.

The feldspar microlites are predominantly potassium-dominated sanidines in the range $Ab_{3–18}Or_{81–98}An_{0–4}$. Most of them are wrapped by a rim of albite to sodium-rich anorthoclase except for those that are embedded in the poikilitic pyroxenes, in which rims are systematically absent.

Pyroxene

Most of the idiomorphic to poikilitic pyroxenes form a continuous trend that lies in the aegirine–augite domain (Figs. 13b, A5, A6). One has to note that the core of pyroxene crystals is usually more calcic than the rim. Compositions range from $Aeg_{43–61}Jd_{3–5}Quad_{35–62}$ for the western margin to $Aeg_{62–71}Jd_{3–5}Quad_{25–33}$ for the more evolved eastern margin (with values within ±0.1; Table A3).

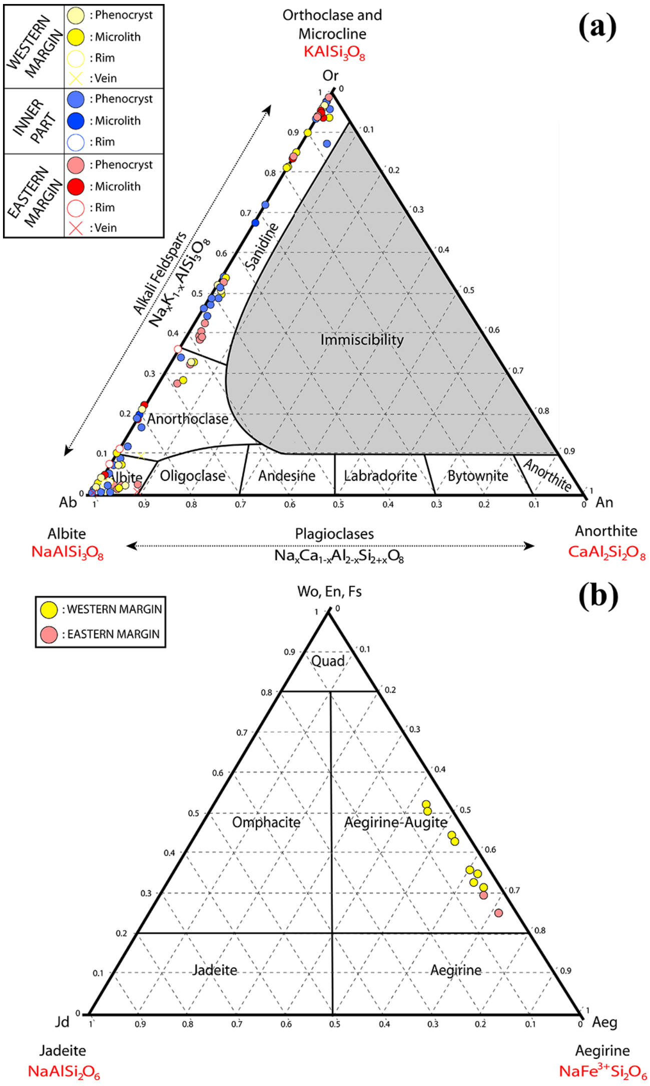

Figure 13. (a) Ternary diagram of feldspars with our data going from the albite pole to the orthoclase pole for phenocrysts, their rim, and the matrix, the veins being exclusively albitic (after Greenwood and Earnshaw, 2012). **(b)** Ternary diagram of Ca–Na and Na pyroxenes with our data from the two margins of the intrusion. "Quad" represents the Ca, Mg, and Fe pyroxene pole with wollastonite (Wo), enstatite (En), and ferrosilite (Fs) after Morimoto (1989). Calculation of the aegirine (Aeg), jadeite (Jd), and Quad poles was determined using the MinPlot program presented by Walters (2022).

Aenigmatite

This mineral is always interstitial and shows a poikilitic texture in the groundmass (Figs. A5, A6). Aenigmatite is common over the intrusion except in the plug area where it is absent. However, this phase is not very abundant in the intrusion, as confirmed by the proportion of titanium in the total rock (0.16 wt %). The average composition is $Na_{1.99}(Fe^{2+}_{3.67}Fe^{3+}_{1.12})Ti_{0.84}Si_{5.83}O_{20}$ for the western margin (with values within ±0.1; Table A4). In general, this mineral phase carries the majority of the titanium present in the tinguaite, not to mention the titanomagnetites.

Magnetite–ulvöspinel solid solution

Iron oxides represent the second Ti-rich mineral phase present over the intrusion as isolated, sometimes poikilitic, grains of less than 50 µm in diameter in the groundmass (Figs. 12c, A5, A6). The largest, idiomorphic and unaltered grains are found in the central area and more particularly in the plug where they have a mean composition of $(Mn_{0.11}Fe^{2+}_{1.13}Fe^{3+}_{1.56})Ti_{0.27}O_4$ (with values within ±0.1; Table A5). In contrast, the oxides become smaller, systematically xenomorphic and acicular with evidence of resorption, and exhibit a composition of $(Mn_{0.19}Fe^{2+}_{1.23}Fe^{3+}_{1.17})Ti_{0.47}O_4$ for the western margin (with values within ±0.1; Table A5).

Feldspathoids

Two feldspathoids have been recognized in the Suc de Sara intrusion (Figs. A5, A6).

Nepheline is the dominant feldspathoid (Fig. 12d) in the intrusion as it is abundant in all facies except at the apex. Nepheline phenocrysts are idiomorphic and exhibit square-shaped sections surrounded by sodium anorthoclase to albite overgrowth ($Ab_{98–80}Or_{2–20}An_{0–9}$). Their average compositions are $Na_{2.87}K_{0.56}Al_{3.55}Si_{4.43}O_{16}$ and $Na_{2.78}K_{0.45}Al_{3.56}Si_{4.52}O_{16}$ for the western and eastern margins, respectively (with values within ±0.1; Table A6). At the core, the few grains present have a composition of $Na_{3.05}K_{0.60}Al_{3.49}Si_{4.41}O_{16}$, a little higher in sodium than the margins.

Sodalite is the secondary feldspathoid in abundance. It is found as small xenomorphic isometric grains in the groundmass (Fig. A5). They are also present as rare and isolated grains in the groundmass of the core. The average composition is $Na_{7.63}(Al_{5.59}Si_{5.83}O_{24})Cl_{1.89}$ for the western margin (with values within ±0.1; Table A7).

Late-magmatic phases

Two minerals – associated with aegirine, aenigmatite, and rare titanomagnetite – that constitute the late-magmatic to hydrothermal assemblages have been recognized (Fig. 14). The first mineral is analcime (Table A8) and belongs to the zeolite group, while the second mineral is låvenite that belongs to the wöhlerite group ($Na_2Ca_2Mn_2Zr_2(Si_2O_7)_2O_2F_2$; Dal Bo et al., 2022). Låvenite and analcime have been determined by WDS analysis, and both minerals were confirmed with Raman spectrum analysis (RRUFF database, ID R040128-analcime and ID R120044-låvenite; Fig. A7). These late-magmatic assemblages fill the voids and the aegirine-rich veins of the phonolite facies near the chilled western margin (SA3; Fig. 13).

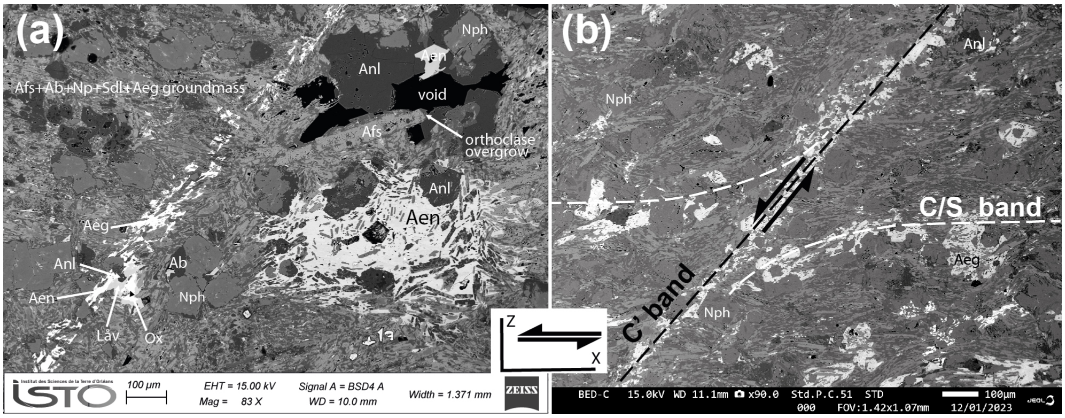

Figure 14. Backscattered electron (BSE) image of the veined phonolite near the western chilled margin (SA3) showing the textural relationships between magmatic and late-magmatic assemblages. $[x, z]$ sections with the lineation x horizontal, sinistral bulk sense of shear. **(a)** The magmatic assemblage is composed of alkali feldspar (Afs), albite (Ab), sodalite (Sdl), and idiomorphic grains of aegirine (Aeg). The late-magmatic assemblage that fills the aegirine-bearing veins is mainly composed of analcime, aenigmatite (Aen), aegirine, låvenite (Lv), and iron oxides (Ox). Aenigmatite appears also as a poikilitic phase in the groundmass, while idiomorphic analcime is present in voids. **(b)** The late-magmatic assemblage fills the anastomosed pattern of veins formed by the C bands parallel to the mineral foliation S and the C′ bands, along which normal synthetic shearing with respect to the bulk sense of shear is highlighted by the bending of the C/S planes.

Analcime constitutes an abundant late-magmatic to hydrothermal hydrous mineral phase present over the intrusion. It is abundant as large idiomorphic crystals in voids and as smaller grains in aegirine-rich veins in particular in the banded phonolite close to the chilled western margin (Fig. 14). Analcime can locally form the most external secondary rim that covers the pre-existing albite rims previously formed around alkali feldspar and nepheline phenocrysts. The average compositions of analcime are $\mathrm{Na_{0.63}Al_{0.99}Si_{2.09}O_6 \cdot H_2O}$ for the western margin and $\mathrm{Na_{0.57}Al_{1.03}Si_{2.08}O_6 \cdot H_2O}$ for the eastern margin (with values within ±0.1; Table A8). For the analcimes present in the core, their average composition is $\mathrm{Na_{0.93}Al_{1.00}Si_{2.01}O_6 \cdot H_2O}$.

The *Låvenite* has been first recognized as a late-magmatic phase in some phonolitic domes of the Velay province by Lacroix (1891) and Batard et al. (1977). This accessory mineral has only been found in the aegirine-bearing vein network that developed near the western margin, together with aegirine, aenigmatite, analcime, and rare oxide (Figs. 14a, A4).

5 Discussion

This work aimed at constraining the modality of segregation and further extraction of the fluid-rich residual melt differentiated during the late-magmatic shallow emplacement stage of the 6.5 Myr old Suc de Sara intrusion. This intrusion was until now considered a ring dyke resulting from the collapse of the roof of a hidden magma chamber causing the ascent at shallower level of a phonolitic magma (Mergoil, 1968; Mergoil and Boivin, 1993). By combining structural measurements at the regional scale and along a complete cross-section of this intrusion, together with petrological analyses and textural observations, we better constrain the model of emplacement and finally emphasize how shear deformation and strain localization structures promote the late-magmatic residual melt segregation that occurred in this differentiated intrusion during its emplacement at shallow depth.

The emplacement model elaborated by Mergoil (1968) considered the Suc de Sara and the Suc de la Veine, whose age remains undetermined, as forming together a unique arched structure. On the other hand, recent mapping suggests that the Suc de la Veine and the Suc de Sara are two different magmatic bodies as they appear not connected (Fig. 3; Defive et al., 2011). Furthermore, Mergoil (1968) pointed out the hypovolcanic nature of the Suc de Sara on the basis of the textural evolution from phaneritic (tinguaite) texture present in the core of the intrusion to aphanitic (phonolite) and ultimately glassy textures approaching the chilled margins (Figs. 7, 8, 10, 11). In addition, sodalite found as an early-magmatic phase forms only at a pressure of less than 150 MPa (Dorado et al., 2021).

5.1 Tectonic context of emplacement of the Suc de Sara intrusion

Palaeotectonic studies (Blès et al., 1989; Mergoil and Boivin, 1993) and recent mapping (Defive et al., 2011) are evidence that associated dextral N080° E–N090° E and sinistral N140° E regional faults were active in a northwest– southeast regional compressional stress field during the late activity of the volcanism in the Boutières graben (Fig. 3a; Blès et al., 1989). In addition, N050° E directed faults are also identified as active during the same period (basaltic dykes, Mergoil and Boivin, 1993). In our fracture analysis performed in the basement we also identified a ∼ N020° E regional fracture network. Obviously, this direction, which corresponds likely to a late Variscan brittle direction observed over the eastern Massif Central (Faure, 1995), was not reactivated during the volcano-tectonic activity of the Cenozoic Velay province. At 6.5 Ma, an opening under a northwest–southeast regional compressional stress of the northern, N140° E striking thick intrusion extended as a thinner, N080° E–N090° E directed dyke to the east, leading to the arced and asymmetric shape of the Suc de Sara body.

Orientations of the S and C structures of the northern part indicate an upward ascent of the magma (Fig. 14b). Moreover, foliation trajectories (Fig. 6) together with the general shape of the intrusion could be interpreted as the transition from a L-shaped dyke, as found in the Lake City caldera in southwestern Colorado (Kennedy et al., 2018), to a neck in a similar geometry to those observed in the Shiprock volcanic complex in New Mexico (Philpotts and Ague, 2009). It should be noted that this model remains compatible with the ring dyke hypothesis of Mergoil (1968), and there is evidence of a geometry well in the nearby Suc des Pradoux intrusion (Fig. 3a; Mergoil and Boivin, 1993). Furthermore, the development of the polygenic breccia along the eastern margin may have resulted from the collapse of the country rock as a roof pendant on top of a hypothetic hidden magmatic chamber, following the model of Mergoil (1968). A simple model including the transition from a dyke to a neck is proposed in Fig. 15a. The two simplified geological sections present the respective position of the Suc des Pradoux and the Suc de Sara as well as the Suc de Sara and the Suc de la Veine (Fig. 15b). These three intrusions are independent.

Our detailed structural measurements including mineral foliation, aegirine- and låvenite-filled shear localization bands, and columnar jointing, when present, are evidence of the asymmetric nature of the architecture of the thicker northwestern part of the intrusion (Fig. 7). This asymmetric structure is synthesized in Fig. 16. First, the asymmetry is well expressed by the position of the axis of this Bingham-shaped plug marked by the nearly horizontal mineral foliation. The axis of this plug is offset towards the western margin (Figs. 7, 16). Second, asymmetry further comes from the two margins that are structurally different. By combining these structural observations with the different mineral assemblages, an evolution from the early-magmatic emplacement to the localized near-solidus shear deformation can be drawn (Fig. 16).

5.2 Early-magmatic mineral assemblages and penetrative fabrics over the intrusion

The early-magmatic assemblage is observed near the margins. It comprises anorthoclase + nepheline + sodalite + aegirine. Orthoclase with evidence of compositional zoning and nepheline are present as both euhedral phenocrysts and microlites. Aegirine + albite ± sodalite are also present in the microlithic groundmass.

This early-magmatic assemblage progressively evolves to compositions with lower Na_2O concentrations toward the plug: nepheline phenocrysts and sodalite microlites are progressively resorbed until their complete disappearance, while anorthoclase phenocrysts are becoming scarce and are all intensively affected by late-magmatic compositional re-equilibration into potassium-rich feldspar (Fig. 16). In contrast, titanomagnetite becomes abundant approaching the plug as idiomorphic unaltered microlites, while it is rare and always strongly resorbed approaching the margins of the intrusion (Fig. 16). The Suc de Sara intrusion is one of the undersaturated magma established in the Velay alkaline series which was recognized by Batard et al. (1977) as an agpaitic phonolite with relict minerals of an initial miaskitic stage such as Ti-bearing oxides (Fig. 3a; Batard et al., 1977; Mergoil and Boivin, 1993). Such peralkaline phonolite was derived either from extensive plagioclase fractionation of an alkali basaltic magma (Marks et al., 2011; Marks and Markl, 2017; Dautria et al., 2004) or from the low degree of partial melting of enriched mantled lithologies at temperatures close to the solidus (Laporte et al., 2014).

The early mineral assemblages exhibit a penetrative planolinear shape fabric characterized by a foliation and a lineation marked by the anorthoclase and aegirine, when present, respectively. This mineral foliation is penetrative over the dyke and displays a curved geometry. However, an asymmetry is noticed as the plug axis, marked by a horizontal foliation, and is closest to the western margin (Fig. 16).

5.3 Late-magmatic to near-solidus mineral assemblages and shear deformation structures

5.3.1 The western margin

West of the plug, and up to a few metres away from the western margin, the tinguaite is characterized by a compositional layering formed by aegirine-rich bands. Magmatic layering is another feature often encountered in agpaitic rocks (Marks and Markl, 2017, and references therein). The formation of this compositional layering could be attributed to the high strain partitioning in the magma that produced D-type shear bands (principal deformation shear bands of Tchalenko, 1968) in which the interstitial melt expressed by poikilitic aegirine was concentrated. Approaching the chilled margin, the thermal gradient was responsible for the transition from the phaneritic to the aphanitic texture (tinguaite to phonolite). The western margin is characterized by a strong mineral foliation parallel to the margin and surrounding rounded alkali feldspar phenocrysts. Progressive transition from D shear bands in the tinguaite to P and Y type (following the terminology of Westerman et al., 2017). Riedel shear bands in the phonolite indicate that the latter was highly crystallized. Such Riedel-type shear bands are com-

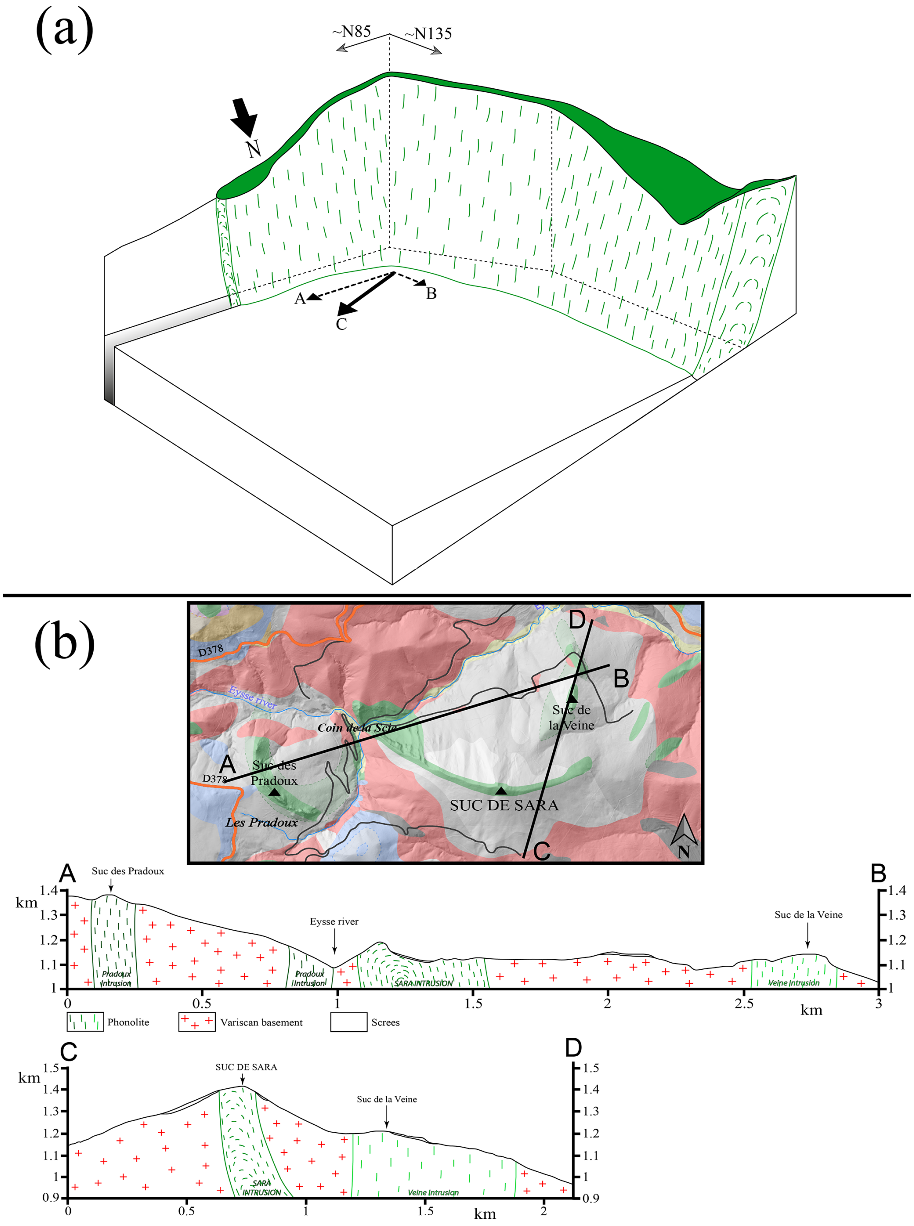

Figure 15. **(a)** 3D model of the Suc de Sara illustrating the shallow emplacement of the phonolitic magma along two associated, ∼ N085° E and ∼ N135° E directed, fractures. Large opening in the ∼ N085° E direction (***A*** vector) conjugate with a small opening in the ∼ N135° E direction (***B*** vector) giving the global opening vector C. **(b)** Synthetic geological sections through the three intrusions of Suc des Pradoux, Suc de Sara, and Suc de la Veine (see also Mergoil and Boivin, 1993). The map is a close-up view from Fig. 3a.

monly developed at the late-magmatic to solid-state transition in sheared magmas by dilatancy (Geshi, 2001; Smith, 2002; Westerman et al., 2017) that promoted late melt segregation in the anastomosed pattern of shear bands (Katz et al., 2006). All these structures point out that the western margin suffered an intense magmatic to late-magmatic upward shearing. In contrast, the preservation of the glassy chilled margin without any associated breccia points out that no brittle, post-magmatic deformation affected the contact with the surrounding gneiss (Figs. 7b, 8). This suggests that the tinguaite accommodated most of, if not all of, the late-magmatic-related shearing.

The interstitial assemblage that developed during the intense strain localization is composed of aegirine + albite ± sodalite, the former having developed as large poikilitic micro-phenocrysts in the groundmass. This assemblage implies a significant Na enrichment of the melt during late crystallization as noticed already for the earlier magmatic assemblage (Marks et al., 2011). Marks and Markl (2017, and reference therein) point out that agpaitic

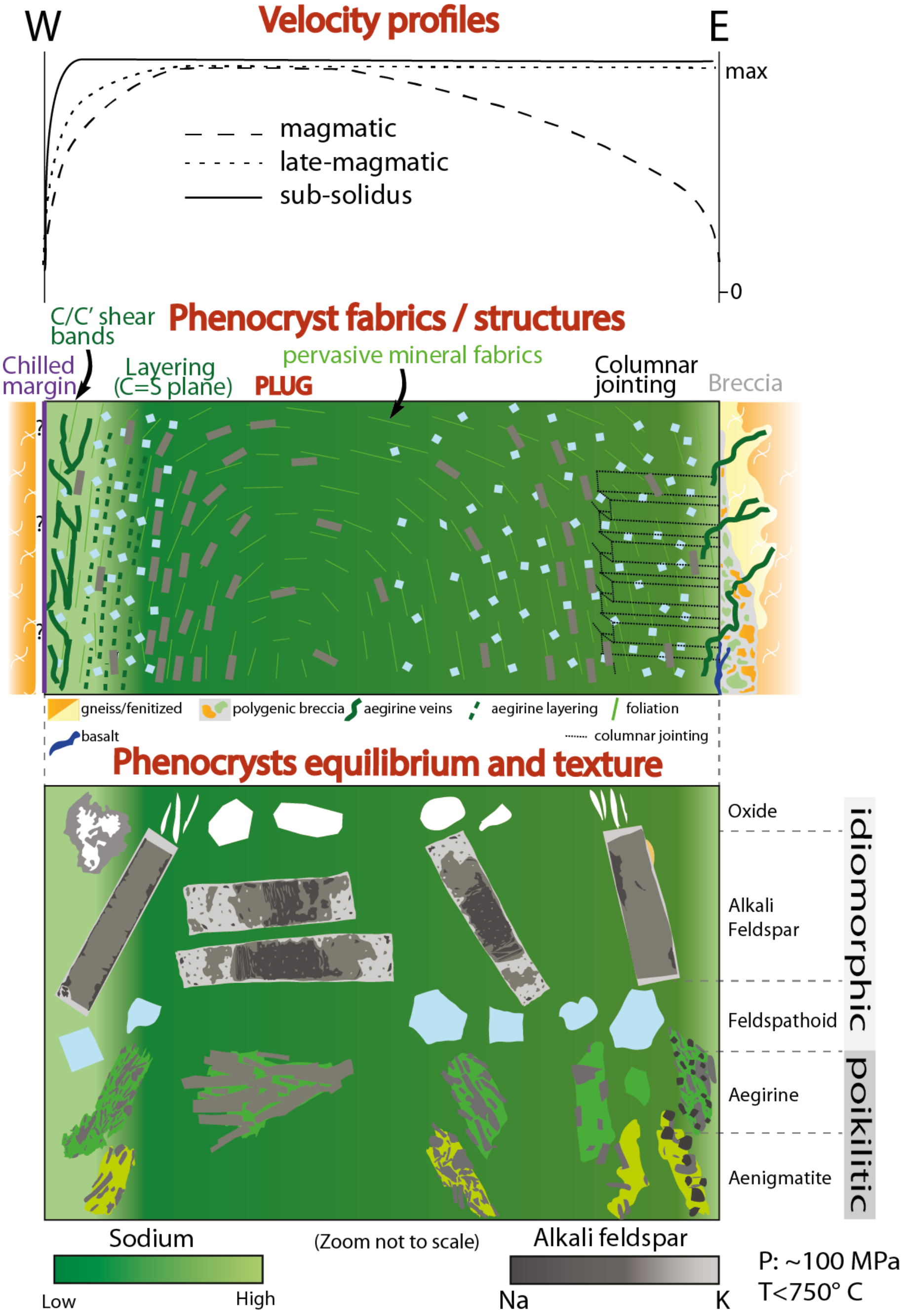

Figure 16. Synthetic scheme of the textural and structural evolution from the magmatic to solid state of the tinguaite. The top diagram shows the schematic evolution of the relative velocity profiles of the ascending magma from the magmatic stage, characterized by an asymmetric curved geometry approaching the margins, to a near-solidus deformation localizing only along the western margin and which results in a plug geometry.

rocks can only form under certain conditions, including reduced crystallization conditions (low $f\mathrm{O}_2$) and relatively dry magmas (low $a_{\mathrm{H_2O}}$). Such conditions allow for later Fe enrichment, increased peralkalinity, halogen retention, and extreme HFSE enrichment in evolving magmas.

The near-solidus assemblage is represented by the growth of analcime over albite on both anorthoclase microlite and nepheline in micro-miarolitic cavities (Chakrabarty et al., 2016; voids in Fig. 14), together with the crystallization of låvenite in aegirine-rich veins. The abundance of miarolitic voids in the vicinity of a well-preserved chilled margin, the abundance of D-type shear bands, and the subsequent C/C′-type shear bands filled by late-magmatic assemblage, together with the pristine nature of the gneiss of the country rock without evidence of Na metasomatism in the vicinity of the contact, are evidence to conclude that the late-magmatic fluids remained mostly confined and segregated in the sheared intrusion near the hanging wall.

5.3.2 The eastern margin

In contrast to the western margin, the eastern margin is characterized by the absence of shear localized structures that could have overprinted the pervasive magmatic shape fabric. In addition, horizontal columnar joints are developed along the contact (Fig. 8e). This shows that the magmatic shearing responsible for the mineral foliation was no longer active at the late-magmatic stage, leading to the development of the horizontal columnar jointing. This could be explained by the asymmetry of the plug that may have promoted the concentration of stress and therefore shear localization in a highly crystalized magma along the closer western margin. However, the presence of a polygenic breccia along the contact with the country rock may indicate that the tinguaite was still ascending as a solid plug along its eastern margin.

The interstitial, late-magmatic assemblage observed in the tinguaite along its eastern margin is similar to that of the western margin. However, this assemblage is restricted to rare, aegirine-rich veins with irregular distribution and orientation, indicating that they consist of fractures possibly opened by excess pore fluid pressure near the solidus conditions. The late-magmatic melt and the Na^+-, Cl^--, H_2O-, and CO_2-rich fluids (Mergoil, 1968; Batard et al., 1977) escaped toward the migmatitic gneiss of the country rock through the highly porous polygenetic breccia. As a consequence, the migmatitic gneiss suffered an intense fenitization characterized by nearly full dequartzification and Na metasomatism (Mergoil, 1968; and Mergoil-Daniel et al., 1986). These authors pointed out the importance of CO_2 in this fenitization process, together with Na-rich fluids. Further evidence of the regional activity of CO_2 is carbonate-rich trachytes and sanidinites found in the Velay province (Hodges, 1991; Batard et al., 1977), as well as in melt inclusion of basanitic lavas in Bas-Vivarais province (Buso et al., 2022).

Most of the very late-magmatic melt and fluids escaped through excess pressure in the bedrock along the eastern margin of the intrusion during its final emplacement. Evidence of this fluid circulation are the rare and irregularly distributed aegirine-rich veins in the tinguaite, the development of a highly porous polygenic breccia instead of a chilled margin, and intensely fenitized bedrock over 8 m thick (Fig. 16).

5.4 Consequences for late melt segregation and extraction in shallow intrusions

The pervasive mineral fabrics are magmatic-flow-related structures (Vernon, 2000; Smith, 2002; Westerman et al., 2017) that developed during the early-magmatic stage during which the amount of melt was sufficiently high to allow for the rotation of phenocrysts and early crystallizing microlites. During this early stage, no melt segregation may arise after crystal settling because the latter is hindered by moderate crystal fraction (Bachmann and Bergantz, 2004; Holness, 2018).

During ascent and subsequent cooling, the microlithic fraction increased and a loose connected framework of crystals – the mush (Bergantz et al., 2017, and references therein) – capable of transmitting emplacement-related magmatic, or tectonic, stress developed. This transition from magmatic flow (liquid-dominated) to stress-directed (solid-dominated) deformation is named the rheologic lock-up threshold (equivalent to the "rigid percolation" threshold of Vigneresse et al., 1996). While the solid fraction continued to increase, the crystal framework stiffened and high localized stress may have led to strain localization (Smith, 1997; Geshi, 2001; Picard et al., 2011). Although the process of initiation of the strain localization in magma, in particular possibly by crystal jamming (Petford, 2009), remains poorly constrained, the onset of shear localized structures such as mineral banding and discrete shear zones is well documented from natural (Arbaret et al., 1993; Smith, 1996; Westerman et al., 2017) and experimental observations (Holtzman and Kohlstedt, 2007; Picard et al., 2011; Laumonier et al., 2011). At medium crystal fraction (almost 40 % to 50 % of solid fraction; Lejeune and Richet, 1995; Picard et al., 2011), shear deformation includes S, C, and C′ bands that may propagate lengthwise from moderate strain and connect to form an anastomosing pattern at high strain (Smith, 1997; Arbaret et al., 2000; Holtzman and Kohlstedt, 2007). Such features are documented along the western margin (Figs. 8, 9). With increasing crystal fraction and/or shear rate, Riedel-type fractures (D, Y, and R type) may develop (Misra et al., 2009). Finally, tensile fractures may arise at sub-solidus conditions, but the process needs relatively high external tectonic load (Bouchez et al., 1992). Tensile fractures have not been observed in the Suc de Sara intrusion, suggesting that final ascent of the magma ended before its full crystallization.

It is well documented that shear localized structures triggered by an external stress field are potential channels for segregation and further extraction of late-magmatic melts and fluids (Geshi, 2001; Holness, 2018, and references therein). In particular, synthetic normal shear bands such as C′ shear bands are the most efficient shear structures for melt segregation because they develop dilatancy (Smith, 1997; Koenders and Petford, 2007; Petford, 2009). As a consequence, residual melt may be sucked from compressional regions of the mush into the local region of negative pressure gradient created by the reorganization of the crystal framework in these dilational shear bands (Petford, 2009). Such behaviour is well expressed along the western margin of the Suc de Sara intrusion. Because of its proximity to the plug, the crystal-rich magma experienced along this margin high shear deformation that resulted in residual Na-rich melt segregation. This segregation, expressed as a mineral banding (C shear bands parallel to the S foliation) in the less-crystalized tinguaite, was progressively replaced laterally by an anastomosing network of dilational C′ shear bands in the cooler, microlite-rich phonolite, approaching the chilled margin (Fig. 14b). Such segregation by localized shear deformation is a common mechanism observed in shallow intrusions (Geshi, 2001) and in lava flows (Smith, 1997). The presence of the chilled margin on the western margin seems to have prevented the extraction of both segregated melt, fluid, and gas that filled the anastomosing network of shear bands toward the country rock, leading to the preservation of an aegirine-rich vein network and miarolitic voids in the intrusion (Fig. 14a).

Oppositely, along the eastern margin the tinguaite did not suffer late-magmatic shear localization as the deformation remained distributed through a significant thickness. The only evidence of the segregation of the residual melt is the presence of rare and randomly oriented aegirine-filled fractures that propagated throughout the polygenic breccia and the country rock. The presence of very low residual porosity in the tinguaite and the pervasive fenitization of the country rock (Mergoil-Daniel et al., 1986; Fig. A4) suggest that extraction of the segregated residual melt and associated Na-rich fluids was efficient along the eastern margin. The process that promoted melt segregation and subsequent extraction toward the country rock remains unconstrained from field observation. Dufek and Bachmann (2010) highlighted a reduction in pore spaces by compaction in a random loose packing of crystals by the self-reorganization of the crystal framework triggered by crystal realignment during magmatic flow (Smith, 2002; Dufek and Bachmann, 2010; Holness, 2018; Hoyos et al., 2022). Such compaction is expected to be the main process acting in moderately crystal-rich mush during shearing by repacking and jamming. These two mechanisms are enhanced for elongated crystals (Hoyos et al., 2022) such as the feldspar microlites forming the groundmass of the tinguaite. Based on this evidence we may expect that, during ascent of the phonolitic magma with a moderately crystallized groundmass, the interstitial differentiated melt may have been forced to migrate toward dilatant areas. Such a process is invoked to explain the dense network of aegirine-rich layers parallel to the main mineral foliation preserved in the tinguaite (Figs. 8b, c, 14b) that experienced high and distributed deformation near the western margin. A similar melt partitioning having developed along the eastern margin, if any, may have been drained thanks to the initiation of fractures generated by near-solidus local excess fluid pressure. These fractures further propagate throughout the permeable polygenic breccia forming the hanging wall of the eastern margin and likely ensure the extraction of the last residual fluids and melts toward the country rock.

6 Conclusion

The 6.5 Myr old Suc de Sara intrusion is the youngest and most differentiated peralkaline phonolite of the Velay volcanic province. It emplaced at shallow depth (< 150 MPa) in the Boutières graben subjected to a northwest–southeast-directed regional compressional stress field.

This intrusion provides an exceptional example of segregation and subsequent extraction of the Na^+-, Cl^--, H_2O-, and CO_2-rich residual melt during magma ascent and final emplacement. Contrasting features of shear deformation between the margins that exhibited different permeabilities highlight the compaction-induced melt segregation as a loose packing of microlites emerged. This segregation further developed as residual melt filling of an anastomosed C/C′ band network in the crystal-rich mush subjected to high shear strain. Subsequent melt extraction throughout the country rock was controlled by the permeability of the hanging wall. Along the western hanging wall of the Suc de Sara intrusion, extraction of the residual melt was prevented by the 15 cm thick chilled margin. In contrast, segregated melt circulated through the highly porous and permeable polygenic breccia and developed along the eastern margin, causing the dequartzification of the country rock and subsequent recrystallization of geodic aegirines in the pores left vacant (Mergoil-Daniel et al., 1986).

Appendix A

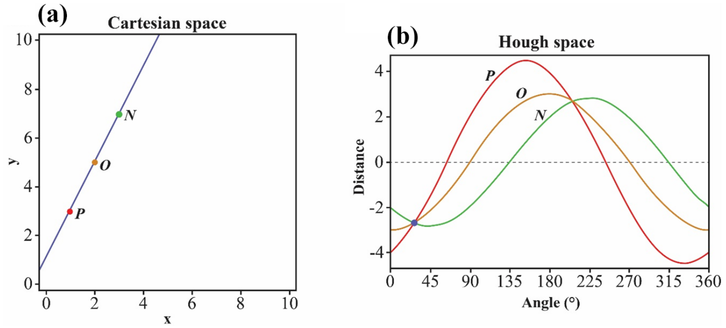

Figure A1. **(a)** Representation of a Cartesian space with three points (N, O, and P) aligned on a straight line. **(b)** Representation of an associated Hough space with the three curves (N, O, and P) corresponding to the points in Cartesian space and a blue point located at the intersection of the curves at $\theta \approx 28°$ and corresponding to the straight line in Cartesian space.

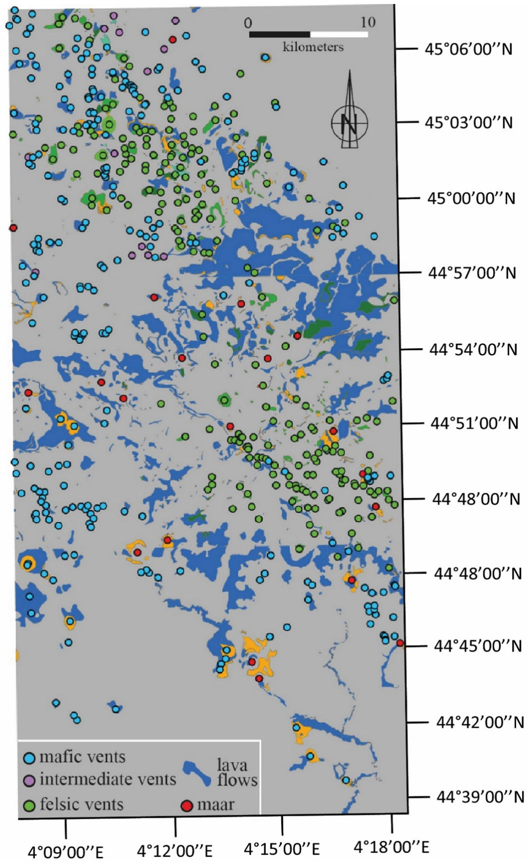

Figure A2. Simplified map of the volcanic formations of the eastern Velay, including the Emblavès and Boutières grabens, with the positions of the 505 vents used for the Hough transform analysis.

Figure A3. **(a)** Polygenic breccia observed on the right bank of the Eysse along the eastern margin between the phonolite and the country rock. **(b)** Lens of basalt emplaced in the solidified phonolite a few metres from the margin.

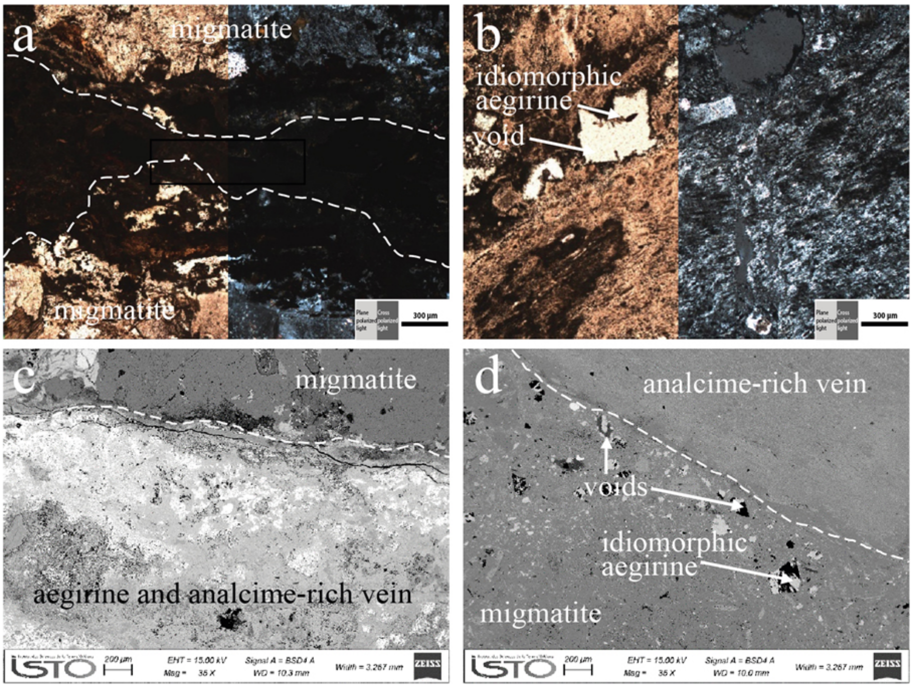

Figure A4. **(a)** A more-marked vein of aegirine in the fenitized migmatite on the eastern margin. **(b)** Breccia on the eastern margin comprising fragments of the host rock and phonolite as well as albite injections. **(c)** SEM image of the more-marked aegirine vein in the fenitized migmatite. **(d)** SEM image of the breccia between the host rock and the phonolite in the Eysse riverbed.

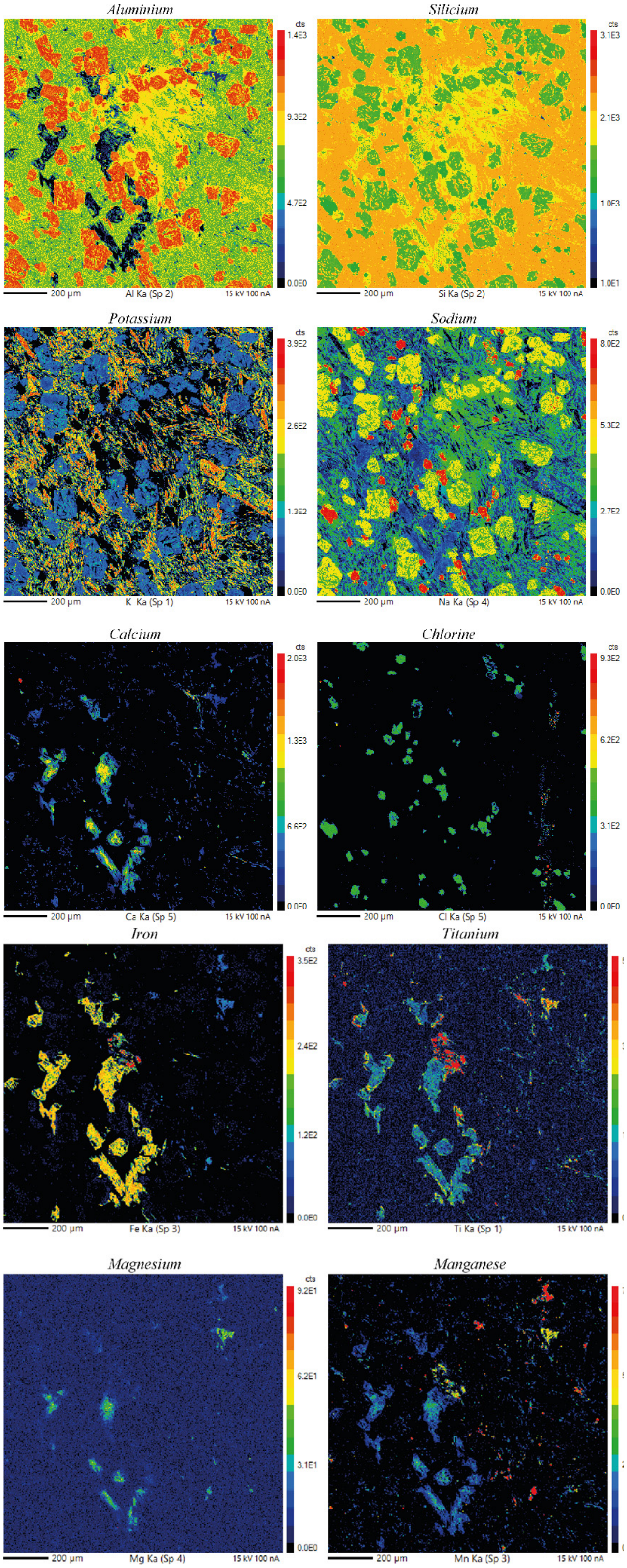

Figure A5. WDS mapping for 10 elements on thin section SA4 (near SA3; western margin). Maps of aluminium, silicium, sodium, and chlorine reveal the presence of feldspathoids. In particular, the sodium and chlorine maps allow us to distinguish between nepheline and sodalite, the latter being richer in sodium and containing chlorine. The potassium map reveals the presence of alkali feldspars. Calcium, iron, and magnesium maps reveal the presence of aegirine. The titanium and iron maps reveal aenigmatite.

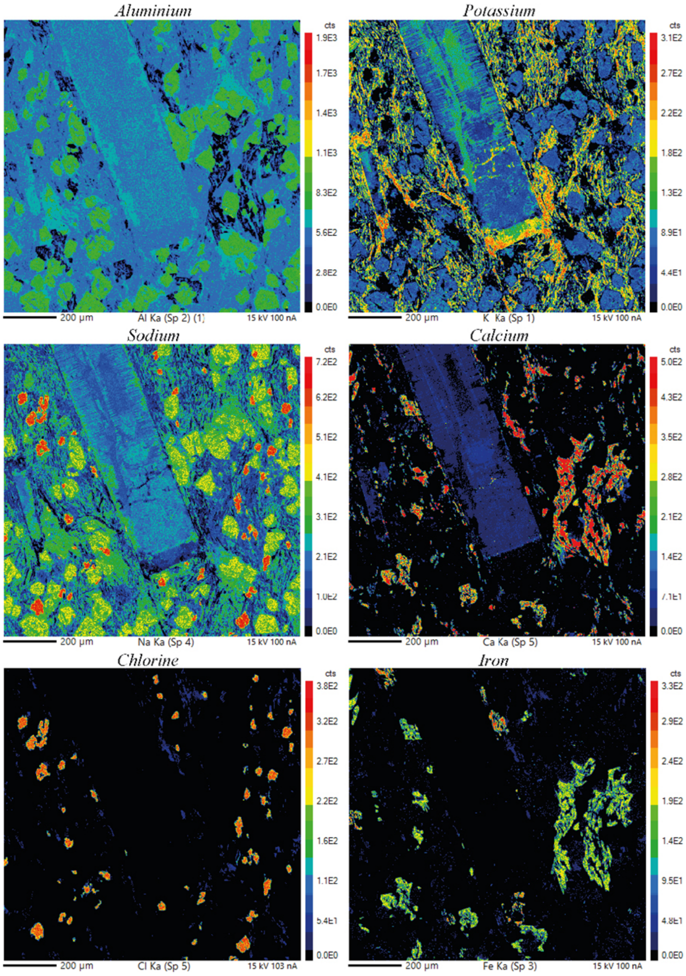

Figure A6. WDS mapping for six elements on thin section SA4 (western margin). These maps reveal the presence of the same minerals as in Fig. A5 but also show variations in composition within an alkali feldspar phenocryst. The potassium-rich overgrowth of this idiomorphic feldspar is clearly visible.

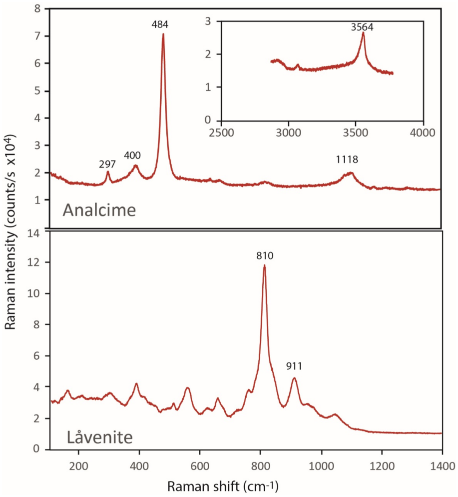

Figure A7. Raman spectra of analcime and låvenite measured in SA3 (see location in Fig. 14a).

Table A1. Representative microprobe analyses of alkali feldspars (in wt %). Total iron is given in FeO. Cation values have been recalculated from the number of oxygens. $\Sigma a = \mathrm{Si} + \mathrm{Al} + \mathrm{Ti}$. $\Sigma b = \mathrm{Fe_{TOT}} + \mathrm{Mn} + \mathrm{Mg} + \mathrm{Ca} + \mathrm{Na} + \mathrm{K}$. The sums (bold font) correspond to the elements that each crystallize in their associated site.

	1	2	3	4	5	6	7	8	9	10	11	12	13	14	15
Sample	SA3	SA3	SA3	SA3	SA5	SA5	SA5	SA5	SA5	SA5	SA5	SA5	SA9	SA9	SA9
SiO_2	66.94	66.65	64.86	65.49	66.90	66.72	66.42	66.72	67.20	67.50	65.74	65.63	65.09	66.58	67.37
TiO_2	0.06	0.00	0.00	0.07	0.00	0.05	0.00	0.00	0.02	0.00	0.03	0.02	0.05	0.05	0.03
Al_2O_3	18.93	19.41	18.53	18.66	19.20	18.68	18.95	19.24	19.02	19.32	18.46	18.46	17.21	19.90	19.54
FeO_{TOT}	0.15	0.02	0.04	0.35	0.35	0.26	0.49	0.03	0.20	0.00	0.15	0.03	0.90	0.09	0.12
MnO	0.00	0.00	0.02	0.07	0.01	0.00	0.02	0.00	0.00	0.00	0.09	0.13	0.01	0.05	0.12
MgO	0.00	0.00	0.00	0.00	0.01	0.02	0.00	0.00	0.00	0.00	0.00	0.01	0.01	0.00	0.01
CaO	0.12	0.20	0.00	0.00	0.08	0.04	0.08	0.15	0.17	0.26	0.00	0.01	0.00	0.64	0.58
Na_2O	6.23	6.63	0.63	2.41	6.38	4.72	7.00	6.63	7.02	7.28	1.08	0.89	0.40	8.10	8.18
K_2O	7.27	7.02	16.28	13.37	6.83	9.75	6.66	7.08	6.35	5.93	14.37	14.80	15.97	4.23	4.25
Total	99.70	99.93	100.36	100.42	99.76	100.24	99.62	99.85	99.98	100.29	99.92	99.98	99.64	99.64	100.20
Number of ions on the basis of eight oxygens															
Si	3.002	2.983	2.990	2.989	2.995	3.005	2.987	2.989	2.999	2.996	3.013	3.011	3.027	2.963	2.981
Ti	0.000	0.000	0.000	0.003	0.000	0.002	0.000	0.000	0.001	0.000	0.001	0.001	0.001	0.002	0.001
Al	1.001	1.024	1.007	1.004	1.013	0.992	1.005	1.016	1.000	1.010	0.997	0.998	0.943	1.044	1.019
$\boldsymbol{\Sigma a}$	**4.003**	**4.007**	**3.997**	**3.996**	**4.008**	**3.999**	**3.992**	**4.005**	**4.000**	**4.006**	**4.011**	**4.010**	**3.971**	**4.009**	**4.001**
Fe_{TOT}	0.005	0.001	0.000	0.004	0.013	0.010	0.000	0.001	0.008	0.000	0.006	0.001	0.035	0.003	0.004
Mn	0.000	0.000	0.001	0.003	0.000	0.000	0.000	0.000	0.000	0.000	0.003	0.001	0.000	0.002	0.005
Mg	0.000	0.000	0.000	0.000	0.000	0.001	0.000	0.000	0.000	0.000	0.000	0.001	0.001	0.000	0.001
Ca	0.006	0.010	0.000	0.000	0.004	0.002	0.040	0.007	0.008	0.012	0.000	0.000	0.000	0.030	0.028
Na	0.542	0.575	0.056	0.213	0.553	0.412	0.610	0.576	0.607	0.626	0.096	0.079	0.036	0.699	0.702
K	0.416	0.401	0.957	0.778	0.390	0.560	0.382	0.405	0.361	0.336	0.840	0.863	0.948	0.240	0.240
$\boldsymbol{\Sigma b}$	**0.969**	**0.987**	**1.014**	**0.998**	**0.960**	**0.985**	**1.032**	**0.989**	**0.984**	**0.974**	**0.945**	**0.945**	**1.020**	**0.974**	**0.980**
Total	4.972	4.994	5.011	4.994	4.968	4.984	5.024	4.994	4.984	4.980	4.956	4.955	4.991	4.983	4.981
(mol %)															
Or	43.2	40.6	94.5	78.5	41.2	57.5	38.4	41.0	37.0	34.3	89.8	91.6	96.4	24.8	24.7
Ab	56.2	58.4	5.5	21.5	58.4	42.3	61.2	58.3	62.2	64.3	10.2	8.4	3.6	72.1	72.4
An	0.6	1.0	0.0	0.0	0.4	0.2	0.4	0.7	0.8	1.2	0.0	0.0	0.0	3.1	2.9

Table A2. Representative microprobe analyses of albites (in wt %).

	1	2	3	4	5
Sample	SA3	SA3	SA3	SA9	SA9
SiO_2	68.58	68.30	68.64	69.07	69.09
TiO_2	0.04	0.05	0.00	0.00	0.00
Al_2O_3	19.92	19.41	19.87	19.92	20.09
FeO_{TOT}	0.10	0.11	0.00	0.09	0.10
MnO	0.00	0.00	0.11	0.00	0.10
MgO	0.00	0.00	0.00	0.00	0.00
CaO	0.59	0.02	0.04	0.00	0.01
Na_2O	11.17	11.28	10.65	11.33	11.01
K_2O	0.15	0.31	0.30	0.47	0.18
Total	100.55	99.48	99.61	100.88	100.58
Number of ions on the basis of eight oxygens					
Si	2.980	2.998	3.000	2.991	2.993
Ti	0.001	0.002	0.000	0.000	0.000
Al	1.021	1.004	1.024	1.017	1.026
Σ*a*	**4.002**	**4.004**	**4.024**	**4.008**	**4.019**
Fe_{TOT}	0.004	0.004	0.000	0.003	0.003
Mn	0.000	0.000	0.004	0.000	0.004
Mg	0.000	0.000	0.000	0.000	0.000
Ca	0.028	0.001	0.002	0.000	0.001
Na	0.941	0.960	0.902	0.951	0.925
K	0.008	0.017	0.016	0.026	0.010
Σ*b*	**0.981**	**0.982**	**0.924**	**0.980**	**0.943**
Total	4.983	4.986	4.948	4.988	4.962
(mol %)					
Or	0.9	1.8	1.8	2.7	1.0
Ab	96.3	98.1	98.0	97.3	98.9
An	2.8	0.1	0.2	0.0	0.1

Table A3. Representative microprobe analyses of pyroxenes (in wt %). $\Sigma a = Si + Al$. $\Sigma b = Al + Ti + Fe^{3+} + Fe^{2+} + Mn + Mg$. $\Sigma c = Ca + Na + K$. Al is distributed so that the sum of the cations at site "a" is as close as possible to two. The Fe^{2+}/Fe^{3+} distinction was made using the method of Droop (1987). The aegirine (Aeg), jadeite (Jd), and Quad (Wo, En, Fs) poles were calculated with the program of Walters (2022).

	1	2	3	4	5	6	7
Sample	SA3	SA3	SA3	SA3	SA3	SA8	SA8
SiO_2	48.56	50.14	47.46	50.62	50.45	50.05	50.62
TiO_2	1.27	0.00	0.00	0.03	0.00	0.93	0.84
Al_2O_3	0.96	0.72	1.15	0.61	0.68	0.85	0.75
FeO_{TOT}	25.95	26.35	25.55	27.11	26.99	28.05	27.77
MnO	2.83	1.14	1.71	0.89	0.82	1.96	1.55
MgO	0.39	0.47	0.56	0.22	0.46	0.34	0.18
CaO	13.53	10.99	14.48	8.48	10.66	8.79	7.19
Na_2O	5.37	7.16	5.06	8.42	7.16	7.91	9.47
K_2O	0.05	0.02	0.00	0.00	0.00	0.05	0.05
Total	98.91	96.99	95.97	96.38	97.22	98.93	98.42
Number of ions on the basis of six oxygens							
Si	2.007	2.089	2.019	2.118	2.096	2.060	2.087
Al	0.000	0.000	0.000	0.000	0.000	0.000	0.000
Σ*a*	**2.007**	**2.089**	**2.019**	**2.118**	**2.096**	**2.060**	**2.087**
Al	0.047	0.035	0.058	0.030	0.034	0.041	0.037
Ti	0.039	0.000	0.000	0.001	0.000	0.029	0.026
Fe^{3+}	0.424	0.524	0.464	0.591	0.506	0.592	0.703
Fe^{2+}	0.441	0.355	0.410	0.311	0.393	0.327	0.199
Mn	0.099	0.040	0.062	0.032	0.029	0.068	0.054
Mg	0.024	0.029	0.036	0.014	0.028	0.021	0.011
Σ*b*	**1.074**	**0.983**	**1.030**	**0.979**	**0.990**	**1.078**	**1.030**
Ca	0.599	0.491	0.660	0.380	0.474	0.388	0.317
Na	0.431	0.578	0.417	0.683	0.577	0.632	0.757
K	0.003	0.001	0.000	0.000	0.000	0.003	0.002
Σ*c*	**1.033**	**1.070**	**1.077**	**1.063**	**1.051**	**1.023**	**1.076**
Total	4.114	4.142	4.126	4.160	4.137	4.161	4.193
(mol %)							
Aeg	42.9	53.2	43.8	61.4	51.8	70.9	62.0
Jd	4.5	3.5	5.2	3.0	3.3	3.5	4.7
Quad	52.6	43.3	51.0	35.6	44.9	25.6	33.3

Table A4. Representative microprobe analyses of aenigmatites (in wt %). $\Sigma a = \mathrm{Si} + \mathrm{Al} + \mathrm{Fe}^{3+}$. $\Sigma b = \mathrm{Al} + \mathrm{Fe}^{3+} + \mathrm{Ti} + \mathrm{Fe}^{2+} + \mathrm{Mn} + \mathrm{Mg} + \mathrm{Ca}$. $\Sigma c = \mathrm{Ca} + \mathrm{Na} + \mathrm{K}$. Al and Fe^{3+} are distributed so that the sum of the cations at site "a" is equal to six.

	1	2	3	4	5
Sample	SA3	SA3	SA3	SA3	SA3
SiO_2	40.33	38.25	38.27	38.96	38.50
TiO_2	7.94	7.87	7.81	7.94	7.22
Al_2O_3	1.09	1.15	1.11	1.00	1.51
FeO_{TOT}	38.84	39.98	39.97	40.32	41.27
MnO	4.58	3.91	4.36	4.38	3.77
MgO	0.11	0.12	0.11	0.08	0.04
CaO	0.35	0.45	0.44	0.30	0.59
Na_2O	7.04	6.99	7.05	6.82	6.84
K_2O	0.07	0.07	0.02	0.00	0.00
Total	100.35	98.79	99.14	99.80	99.74
Number of ions on the basis of 20 oxygens					
Si	5.832	5.683	5.693	5.724	5.680
Al	0.168	0.202	0.193	0.173	0.262
Fe^{3+}	0.000	0.115	0.114	0.103	0.058
Σa	**6.000**	**6.000**	**6.000**	**6.000**	**6.000**
Al	0.019	0.000	0.000	0.000	0.000
Fe^{3+}	0.573	0.859	0.877	0.691	0.962
Ti	0.864	0.880	0.872	0.878	0.801
Fe^{2+}	4.058	3.873	3.810	4.063	3.943
Mn	0.561	0.493	0.548	0.545	0.472
Mg	0.023	0.026	0.023	0.017	0.009
Ca	0.000	0.000	0.000	0.000	0.000
Σb	**6.098**	**6.131**	**6.130**	**6.194**	**6.187**
Ca	0.053	0.071	0.071	0.047	0.093
Na	1.973	2.013	2.029	1.944	1.957
K	0.012	0.013	0.004	0.000	0.000
Σc	**2.038**	**2.097**	**2.104**	**1.991**	**2.050**
Total	14.136	14.228	14.234	14.185	14.237

Table A5. Representative microprobe analyses of magnetite–ulvöspinels (in wt %). $\Sigma a = \mathrm{Si} + \mathrm{Ti} + \mathrm{Al}$. $\Sigma b = \mathrm{Fe}^{3+} + \mathrm{Fe}^{2+} + \mathrm{Mn} + \mathrm{Mg} + \mathrm{Ca} + \mathrm{Na} + \mathrm{K}$.

	1	2	3
Sample	SA3	SA5	SA5
SiO_2	0.02	0.10	0.11
TiO_2	14.06	7.43	7.66
Al_2O_3	0.76	0.15	0.18
FeO_{TOT}	76.18	83.84	85.54
MnO	5.02	2.71	2.90
MgO	0.04	0.00	0.00
CaO	0.02	0.03	0.02
Na_2O	0.03	0.00	0.00
K_2O	0.03	0.00	0.00
Total	96.16	94.26	96.41
Number of ions on the basis of 32 oxygens			
Si	0.007	0.040	0.041
Ti	3.734	2.126	2.141
Al	0.316	0.066	0.079
Σa	**4.057**	**2.232**	**2.261**
Fe^{3+}	9.372	12.459	12.419
Fe^{2+}	9.829	9.031	9.015
Mn	1.502	0.874	0.914
Mg	0.023	0.000	0.002
Ca	0.007	0.010	0.008
Na	0.022	0.000	0.000
K	0.000	0.000	0.000
Σb	**20.755**	**22.374**	**22.358**
Total	24.812	24.606	24.619

Table A6. Representative microprobe analyses of nephelines (in wt %). $\Sigma a = \mathrm{Si} + \mathrm{Ti} + \mathrm{Al}$. $\Sigma b = \mathrm{Fe_{TOT}} + \mathrm{Mn} + \mathrm{Mg} + \mathrm{Ca} + \mathrm{Na} + \mathrm{K}$.

	1	2	3	4	5	6	7	8	9	10	11	12	13
Sample	SA3	SA3	SA3	SA3	SA3	SA3	SA3	SA3	SA3	SA5	SA5	SA5	SA5
SiO_2	45.98	46.85	45.89	48.97	47.48	46.09	46.62	45.62	47.78	44.99	47.42	45.47	45.64
TiO_2	0.09	0.03	0.00	0.00	0.00	0.06	0.00	0.00	0.00	0.09	0.00	0.00	0.17
Al_2O_3	33.59	32.53	32.06	30.41	31.09	32.06	32.87	31.32	29.97	31.00	30.16	31.15	31.06
FeO_{TOT}	1.01	1.27	1.32	1.13	0.96	1.33	1.24	1.07	1.31	1.49	1.10	1.15	1.59
MnO	0.08	0.00	0.02	0.03	0.04	0.01	0.00	0.03	0.00	0.04	0.06	0.00	0.00
MgO	0.03	0.00	0.01	0.02	0.00	0.01	0.00	0.00	0.01	0.00	0.01	0.00	0.01
CaO	0.00	0.01	0.00	0.00	0.00	0.01	0.00	0.04	0.06	0.07	0.00	0.00	0.00
Na_2O	14.37	13.64	16.52	16.05	16.39	15.89	14.85	16.38	16.30	16.19	16.21	16.47	16.51
K_2O	5.42	4.80	5.16	3.36	4.40	4.97	4.56	4.99	4.00	5.28	4.13	5.00	5.10
Total	100.57	99.13	100.98	99.97	100.36	100.43	100.14	99.45	99.43	99.15	99.09	99.24	100.08
Number of ions on the basis of 32 oxygens													
Si	8.664	8.892	8.695	9.196	8.966	8.744	8.791	8.760	9.097	8.707	9.059	8.758	8.742
Ti	0.012	0.004	0.000	0.000	0.000	0.009	0.000	0.000	0.000	0.013	0.000	0.000	0.025
Al	7.461	7.277	7.159	6.731	6.920	7.168	7.306	7.089	6.726	7.072	6.971	7.072	7.013
Σa	**16.137**	**16.173**	**15.854**	**15.927**	**15.886**	**15.921**	**16.097**	**15.849**	**15.823**	**15.792**	**16.030**	**15.830**	**15.780**
Fe_{TOT}	0.159	0.202	0.210	0.177	0.152	0.211	0.195	0.171	0.209	0.241	0.176	0.185	0.255
Mn	0.013	0.000	0.003	0.004	0.006	0.002	0.000	0.005	0.000	0.007	0.010	0.000	0.000
Mg	0.007	0.000	0.002	0.006	0.000	0.002	0.000	0.001	0.002	0.000	0.002	0.000	0.002
Ca	0.000	0.001	0.000	0.000	0.000	0.002	0.000	0.009	0.012	0.015	0.000	0.000	0.000
Na	5.252	5.019	6.068	5.843	6.003	5.847	5.428	6.099	6.018	6.076	6.005	6.151	6.132
K	1.303	1.162	1.248	0.805	1.059	1.204	1.098	1.222	0.972	1.304	1.007	1.229	1.246
Σb	**6.734**	**6.384**	**7.531**	**6.835**	**7.220**	**7.268**	**6.721**	**7.507**	**7.213**	**7.643**	**7.200**	**7.565**	7.635
Total	22.871	22.557	23.385	22.762	23.106	23.189	22.818	23.356	23.036	23.435	23.230	23.395	23.415

Table A7. Representative microprobe analyses of sodalites (in wt %). $\Sigma a = \mathrm{Si} + \mathrm{Ti} + \mathrm{Al}$. $\Sigma b = \mathrm{Fe_{TOT}} + \mathrm{Mn} + \mathrm{Mg} + \mathrm{Ca} + \mathrm{Na} + \mathrm{K} + \mathrm{Cl}$.

	1	2	3	4	5	6	7
Sample	SA3	SA3	SA3	SA3	SA3	SA3	SA3
SiO_2	36.76	36.61	36.47	36.94	37.76	36.97	37.70
TiO_2	0.00	0.03	0.02	0.03	0.02	0.06	0.08
Al_2O_3	30.08	29.68	29.47	29.95	30.77	30.63	30.21
FeO_{TOT}	0.80	1.07	1.03	1.17	0.51	0.66	0.64
MnO	0.01	0.05	0.06	0.05	0.01	0.02	0.07
MgO	0.00	0.00	0.00	0.00	0.00	0.00	0.00
CaO	0.00	0.00	0.02	0.08	0.00	0.07	0.00
Na_2O	25.28	25.47	24.80	25.02	25.71	23.61	24.87
K_2O	0.07	0.07	0.10	0.06	0.11	0.06	0.03
Cl	7.05	7.13	7.01	7.08	6.91	6.96	7.33
Total	100.05	100.11	98.98	100.38	101.80	99.04	100.93
Number of ions on the basis of 24 oxygens							
Si	5.807	5.803	5.831	5.822	5.833	5.847	5.888
Ti	0.000	0.003	0.002	0.004	0.002	0.007	0.009
Al	5.601	5.545	5.553	5.564	5.602	5.710	5.562
Σa	**11.408**	**11.351**	**11.386**	**11.390**	**11.437**	**11.564**	**11.459**
Fe_{TOT}	0.105	0.142	0.138	0.155	0.066	0.087	0.083
Mn	0.002	0.006	0.009	0.007	0.001	0.002	0.009
Mg	0.000	0.000	0.000	0.000	0.000	0.000	0.000
Ca	0.000	0.000	0.003	0.013	0.000	0.012	0.000
Na	7.743	7.828	7.688	7.646	7.700	7.240	7.532
K	0.015	0.015	0.020	0.012	0.021	0.012	0.007
Cl	1.889	1.916	1.900	1.891	1.809	1.866	1.940
Σb	**9.754**	**9.907**	**9.758**	**9.724**	**9.597**	**9.219**	**9.571**
Total	21.162	21.258	21.144	21.114	21.034	20.783	21.030

Table A8. Representative microprobe analyses of analcimes (in wt %). $\Sigma a = \mathrm{Si} + \mathrm{Ti} + \mathrm{Al}$. $\Sigma b = \mathrm{Fe_{TOT}} + \mathrm{Mn} + \mathrm{Mg} + \mathrm{Ca} + \mathrm{Na} + \mathrm{K}$. Water is not analysed (n.d.: no data).

	1	2	3	4	5	6	7	8	9	10	11
Sample	SA3	SA3	SA3	SA3	SA3	SA5	SA5	SA5	SA5	SA5	SA9
SiO_2	56.63	56.44	58.04	56.88	57.91	54.43	52.80	53.94	53.90	54.99	57.58
TiO_2	0.00	0.00	0.08	0.03	0.03	0.00	0.01	0.00	0.00	0.00	0.00
Al_2O_3	22.89	22.51	22.20	23.73	24.00	23.07	22.48	23.03	22.64	23.37	24.32
FeO_{TOT}	0.00	0.07	0.17	0.25	0.29	0.06	0.08	0.21	0.00	0.36	0.11
MnO	0.00	0.00	0.03	0.03	0.10	0.01	0.04	0.00	0.00	0.00	0.00
MgO	0.00	0.01	0.02	0.01	0.00	0.00	0.00	0.00	0.00	0.00	0.03
CaO	0.02	0.03	0.02	0.54	0.01	0.01	0.00	0.00	0.01	0.00	0.13
Na_2O	9.13	10.13	9.30	8.40	7.64	12.78	13.51	13.09	13.34	11.90	8.18
K_2O	0.15	0.15	0.06	0.19	2.03	0.08	0.14	0.16	0.08	0.08	0.17
H_2O	n.d.	n.d.	n.d.	n.d.	n.d.	n.d.	n.d.	n.d.	n.d.	n.d.	n.d.
Total	88.82	89.34	89.92	90.06	92.01	90.44	89.06	90.43	89.97	90.70	90.52
Number of ions on the basis of 96 framework oxygens											
Si	33.415	33.300	33.825	33.124	33.221	32.220	31.948	32.047	32.175	32.350	33.202
Ti	0.000	0.000	0.037	0.014	0.013	0.000	0.005	0.000	0.000	0.000	0.000
Al	15.919	15.658	15.248	16.287	16.231	16.099	16.033	16.132	15.930	16.205	16.532
Σa	**49.334**	**48.958**	**49.110**	**49.425**	**49.465**	**48.319**	**47.986**	**48.179**	**48.105**	**48.555**	**49.734**
Fe_{TOT}	0.000	0.035	0.082	0.119	0.140	0.030	0.043	0.104	0.000	0.177	0.052
Mn	0.000	0.000	0.014	0.016	0.048	0.008	0.020	0.000	0.000	0.000	0.000
Mg	0.000	0.005	0.018	0.012	0.000	0.000	0.000	0.000	0.001	0.000	0.026
Ca	0.011	0.022	0.010	0.336	0.005	0.008	0.000	0.003	0.006	0.000	0.080
Na	10.448	11.585	10.515	9.481	8.501	14.674	15.856	15.080	15.438	13.572	9.151
K	0.110	0.116	0.045	0.140	1.487	0.062	0.107	0.121	0.059	0.056	0.128
Σb	**10.569**	**11.763**	**10.684**	**10.104**	**10.181**	**14.782**	**16.026**	**15.308**	**15.504**	**13.805**	**9.437**
H_2O	n.d.	n.d.	n.d.	n.d.	n.d.	n.d.	n.d.	n.d.	n.d.	n.d.	n.d.
Total	59.903	60.721	59.794	59.529	59.646	63.101	64.012	63.487	63.609	62.360	59.171

Code and data availability. All data derived from this research are presented in the enclosed tables, the figures, and the Appendix. The code developed by Thomas Pereira and Gautier Laurent for the Hough transformation is available at the following link: https://doi.org/10.5281/zenodo.11469645 (Laurent, 2024).

Author contributions. TP: structural measurements and treatment, sampling, petrology, writing of the original draft. LA: structural measurements, funding acquisition, project administration, writing of the original draft. JA: petrology. ML: sampling, petrology, geochemistry. MS: sampling, petrology. CG: structural measurements, linear analysis, SIG conceptualization. GL: alignment analysis, Hough transform software. AS: Raman analysis. IDC: petrology.

Competing interests. The contact author has declared that none of the authors has any competing interests.

Special issue statement. This article is part of the special issue "Probing the Earth: magma and fluids, a tribute to the career of Michel Pichavant". It is a result of the Magma & Fluids workshop, Orléans, France, 4–6 July 2022.

Acknowledgements. The authors thanks Emma Saulnier and Geoffroy Rodrik for their contribution to the lineament analysis. This project has benefited from the expertise and the facilities of the Platform MACLE – CVL which was co-funded by the European Union and Centre-Val de Loire region (FEDER). We thank François Holtz for his editorial handling and Michael Marks and Armel Menant for their comments that improved the manuscript.

Financial support. This research has been supported by the French Agency for Research (Agence Nationale de la Recherche, ANR) through the grant MECAMUSH ANR-19-CE0315-0007.

Review statement. This paper was edited by Francois Holtz and reviewed by Armel Menant, Michael Marks, and Francois Holtz.

References

Ablay, G. J., Carroll, M. R., Palmer, M. R., Marti, J., and Sparks, R. S. J.: Basanite-phonolite lineage of the Teide-Pico Viejo Volcanic Complex, Tenerife, Canary Islands, J. Petrol., 39, 905–936, 1998.

Allan, A. S., Morgan, D. J., Wilson, C. J., and Millet, M. A.: From mush to eruption in centuries: assembly of the super-sized Oruanui magma body, Contrib. Mineral. Petr., 166, 143–164, 2013.

Arbaret, L., Diot, H., and Launeau, P.: Le suc phonolitique du Petit Gerbier (Velay, Massif Central); fabriques magnétiques et magmatique, C.R. Acad. Sci. Paris, 316, 1603–1610, 1993.

Arbaret, L., Burg, J. P., Zeilinger, G., Chaudhry, N., Hussain, S., and Dawood, H.: Pre-collisional anastomosing shear zones in the Kohistan arc, NW Pakistan, Geol. Soc. Lond. Spec. Publ., 170, 295–311, 2000.

Bachmann, O. and Bergantz, G. W.: On the origin of crystal-poor rhyolites: extracted from batholithic crystal mushes, J. Petrol., 45, 1565–1582, 2004.

Bachmann, O. and Bergantz, G. W.: The magma reservoirs that feed supereruptions, Elements, 4, 17–21, 2008.

Bambier, A., Berger, E., Mergoil, J., Valadas, B., Veyret, Y., and Weisbrod, A.: Carte géologique de la France à 1/50000 (840), 1985.

Barbey, P., Villaros, A., Marignac, C., and Montel, J. M.: Multiphase melting, magma emplacement and PT-time path in late-collisional context: the Velay example (Massif Central, France), B. Soc. Géol. Fr., 186, 93–116, 2015.

Batard, F.: Les feldspaths dans les roches volcaniques différenciées du Massif Central Français, Thèse 3e cycle, Univ. Clermont-Ferrand, 176 pp., GEODEBRGMFR0741834, 1974.

Batard, F., Mergoil-Daniel, J., and Mergoil, J.: Calcite et rôle possible du CO_2 dans la genèse des roches hyperalcalines et agpaïtiques du Velay oriental (Haute-Loire, Massif central français), B. Minéral., 100, 343–347, 1977.

Bergantz, G. W., Schleicher, J. M., and Burgisser, A.: On the kinematics and dynamics of crystal-rich systems, J. Geophys. Res.-Sol. Ea., 122, 6131–6159, 2017.

Berger, E. T. and Vannier, M.: Petrology of Megacrysts, Mafic and Ultramafic Xenoliths from the Pipe of Eglazines, Causses, France, In Developments in Petrology, Elsevier 11A, 155–168, https://doi.org/10.1016/B978-0-444-42273-6.50019-5, 1984.

Blès, J. L., Bonijoly, D., Castaing, C., and Gros, Y.: Successive post-Variscan stress fields in the French Massif Central and its borders (Western European plate): comparison with geodynamic data, Tectonophysics, 169, 79–111, 1989.

Boivin, P., Besson, J. C., Briot, D., Camus, G., Goër, A. de, Gourgaud, A., Labazuy, P., de Larouzière, F. D., Livet, M., Mergoil, J., Miallier, D., Morel, J. M., Vernet, G., and Vincent, P.: Volcanologie de la Chaîne des Puys, Carte et fascicule, 4th Edn., Parc Naturel des Volcans d'Auvergne, 179 pp., 2004.

Bouchez, J. L., Delas, C., Gleizes, G., Nédélec, A., and Cuney, M.: Submagmatic microfractures in granites, Geology, 20, 35–38, 1992.

Bout, P.: Histoire géologique et morphogenèse du système Velay SE-Boutières-Coiron, Rev. Geogr. Phys. Geol., 2, 225–251, 1966.

Burgisser, A. and Bergantz, G. W.: A rapid mechanism to remobilize and homogenize highly crystalline magma bodies, Nature, 471, 212–215, 2011.

Buso, R., Laporte, D., Schiavi, F., Cluzel, N., and Fonquernie, C.: High-pressure homogenization of olivine-hosted CO_2-rich melt inclusions in a piston cylinder: insight into the volatile content of primary mantle melts, Eur. J. Mineral., 34, 325–349, https://doi.org/10.5194/ejm-34-325-2022, 2022.

Cashman, K. V., Sparks, R. S. J., and Blundy, J. D.: Vertically extensive and unstable magmatic systems: a unified view of igneous processes, Science, 355, 6331, https://doi.org/10.1126/science.aag3055, 2017.

Chakrabarty, A., Mitchell, R. H., Ren, M., Saha, P. K., Pal, S., Pruseth, K. L., and Sen, A. K.: Magmatic, hydrothermal and subsolidus evolution of the agpaitic nepheline syenites of the Sushina Hill Complex, India: implications for the metamorphism of peralkaline syenites, Mineral. Mag., 80, 1161–1193, 2016.

Couzinié, S., Moyen, J. F., Villaros, A., Paquette, J. L., Scarrow, J. H., and Marignac, C.: Temporal relationships between Mg-K mafic magmatism and catastrophic melting of the Variscan crust in the southern part of the Velay Complex (Massif Central, France), J. Geosci., 59, 69–86, 2014.

Dal Bo, F., Friis, H., and Mills, S. J.: Nomenclature of wöhlerite-group minerals, Mineral. Mag., 86, 661–676, 2022.

Dautria, J. M., Liotard, J. M., and Briot, D.: Particularités de la contamination crustale des phonolites : exemple du Velay oriental (Massif Central), C.R. Géosci., 336, 971–981, https://doi.org/10.1016/j.crte.2004.03.006, 2004.

Defive, E., Courrioux, G., Ledru, P., Poiraud, A., and Prognon, C.: Carte géologique de la France (1/50000), feuille Le Monastier-sur-Gazeille no. 816, BRGM, Orléans, hal-01131052, version 1, 2011.

Delph, J. R., Ward, K. M., Zandt, G., Ducea, M. N., and Beck, S. L.: Imaging a magma plumbing system from MASH zone to magma reservoir, Earth Planet. Sc. Lett., 457, 313–324, 2017.

Dorado, O., Andújar, J., Martí, J., and Geyer, A.: Pre-eruptive conditions at satellite vent eruptions at Teide-Pico Viejo complex (Tenerife, Canary Islands), Lithos, 396–397, 106193, https://doi.org/10.1016/j.lithos.2021.106193, 2021.

Droop, G. T. R.: A general equation for estimating Fe^{3+} concentrations in ferromagnesian silicates and oxides from microprobe analyses, using stoichiometric criteria, Mineral. Mag., 51, 431–435, 1987.

Dufek, J. and Bachmann, O.: Quantum magmatism: Magmatic compositional gaps generated by melt-crystal dynamics, Geology, 38, 687–690, 2010.

Dupraz, J., and Didier, J.: Le complexe anatectique du Velay (Massif central): structure d'ensemble et évolution géologique, 74–87, Géologie de la France, no. 4, BRGM, 7204465, 1988.

Faure, M.: Late orogenic carboniferous extensions in the Variscan French Massif Central, Tectonics, 14, 132–153, 1995.

Geshi, N.: Melt segregation by localized shear deformation and fracturing during crystallization of magma in shallow intrusions of the Otoge volcanic complex, central Japan, J. Volcanol. Geoth. Res., 106, 285–300, 2001.

Girod, M., Bouiller, R., Roche, A., Weber, F., Larque, P., Giot, D., Guerin, C., Bladier, Y., Laurent, P., and Bambier, A.: Geological map, 1 : 50000; no. 791, XXVII-35, 31 pp., H.T. 1, Bibl. 2 pp., 4 Ill., 1 CART. Univ. Claude Bernard, Paris, France, 1979.

Greenwood, N. N. and Earnshaw, A.: Chemistry of the Elements, Elsevier, 1600 pp., ISBN 0080501095, 2012.

Hart, P. E. and Duda, R. O.: Use of the Hough transformation to detect lines and curves in pictures, Communications of the ACMk, 15, 11–15, 1972.

Hodges, S.: Petrogenesis of the phonolitic rocks of the Velay Oriental, France, Thèse PhD, Oxford Univ, Vol. 1, 1–207, 1991.

Holness, M. B.: Melt segregation from silicic crystal mushes: a critical appraisal of possible mechanisms and their microstructural record, Contrib. Mineral. Petr., 173, 48, https://doi.org/10.1007/s00410-018-1465-2, 2018.

Holtzman, B. K. and Kohlstedt, D. L.: Stress-driven melt segregation and strain partitioning in partially molten rocks: Effects of stress and strain, J. Petrol., 48, 2379–2406, 2007.

Hough, P. V. C.: Machine analysis of bubble chamber pictures, Proc. of the International Conference on High Energy Accelerators and Instrumentation, September 1959, Geneva, Switzerland, 554–556, 1959.

Hoyos, S., Florez, D., Pec, M., and Huber, C.: Crystal Shape Control on the Repacking and Jamming of Crystal-Rich Mushes, Geophys. Res. Lett., 49, e2022GL100040, https://doi.org/10.1029/2022GL100040, 2022.

Jeffery, A. J. and Gertisser, R.: Peralkaline felsic magmatism of the Atlantic islands, Front. Earth Sci., 6, 145, https://doi.org/10.3389/feart.2018.00145, 2018.

Jung, J.: Géologie, Géomorphologie et Structure Profonde du Massif Central Français, Plein Air Service, Éditions Scientifiques, 358–363, 1971.

Katz, R. F., Spiegelman, M., and Holtzman, B.: The dynamics of melt and shear localization in partially molten aggregates, Nature, 442, 676–679, 2006.

Kennedy, B. M., Holohan, E. P., Stix, J., Gravley, D. M., Davidson, J. R., Cole, J. W., and Burchardt S.: Volcanic and igneous plumbing systems of caldera volcanoes, in: Volcanic and Igneous Plumbing Systems, Elsevier, 259–284, https://doi.org/10.1016/B978-0-12-809749-6.00010-8, 2018.

Koenders, M. A. and Petford, N.: Shear-induced pressure changes and seepage phenomena in a deforming porous layer-III, Geophys. J. Int., 171, 943–953, 2007.

Lacroix, A.: Sur l'existence de la låvénite dans les phonolites néphéliniques de la Haute-Loire, B.éral., 14, 15–16, 1891.

Laporte, D., Lambart, S., Schiano, P., and Ottolini, L.: Experimental derivation of nepheline syenite and phonolite liquids by partial melting of upper mantle peridotites, Earth Planet. Sc. Lett., 404, 319–331, 2014.

Laumonier, M., Arbaret, L., Burgisser, A., and Champallier, R.: Porosity redistribution enhanced by strain localization in crystal-rich magmas, Geology, 39, 715–718, 2011.

Le Bas, M. J., Le Maitre, R. W., Streickeisen, A., and Zanettin, B.: A classification of igneous rocks and glossary terms, IUGS and Blackwell Sientific Pub., https://doi.org/10.1093/petrology/27.3.745, 1986.

Legendre, C., Maury, R. C., Caroff, M., Guillou, H., Cotton, J., Chauvel, C., Bollinger, C., Hémond, C., Guille, G., Blais, S., Rossi, P., and Savanier, D.: Origin of exceptionally abundant phonolites on Ua Pou island (Marquesas, French Polynesia): partial melting of basanites followed by crustal contamination, J. Petrol., 46, 1925–1962, 2005.

Lejeune, A. M. and Richet, P.: Rheology of crystal-bearing silicate melts: An experimental study at high viscosities, J. Geophys. Res.-Sol. Ea., 100, 4215–4229, 1995.

Macdonald, R., White, J. C., and Belkin, H. E.: Peralkaline silicic extrusive rocks: magma genesis, evolution, plumbing systems and eruption, C.R. Géosci., 353. 7–59, 2021.

Malcles, O., Vernant, P., Chéry, J., Camps, P., Cazes, G., Ritz, J.-F., and Fink, D.: Determining the Plio-Quaternary uplift of the southern French Massif Central; a new insight for intraplate orogen dynamics, Solid Earth, 11, 241–258, https://doi.org/10.5194/se-11-241-2020, 2020.

Marks, M. A. and Markl, G.: A global review on agpaitic rocks, Earth-Sci. Rev., 173, 229–258, 2017.

Marks, M. A., Hettmann, K., Schilling, J., Frost, B. R., and Markl, G.: The mineralogical diversity of alkaline igneous rocks: critical factors for the transition from miaskitic to agpaitic phase assemblages, J. Petrol., 52, 439–455, 2011.

Maury, R. C. and Varet, J.: Le volcanisme tertiaire et quaternaire de France, 26th Int. Geol. Congr., Paris, 7–17 July 1980, BRGM, 3, 142, 1980.

Martin, A. M., Médard, E., Righter, K., and Lanzirotti, A.: Intraplate mantle oxidation by volatile-rich silicic magmas, Lithos, 292, 320–333, 2017.

Mergoil, J.: Gisement en filons annulaires de phonolites du Velay (Massif Central français), C.R. Acad. Sci. Paris, 267, 12–14, 1968.

Mergoil, J. and Boivin, P.: Le Velay: Son volcanisme et les formations associées, Notice de la carte à 1/100 000, Géologie de la France, no. 3, 3–96, 1993.

Mergoil-Daniel, J., Labernardière, H., and Maisonneuve, J.: Épisyénites-fenites et source de l'uranium, C.R. Acad. Sci. Paris, 302, 227–232, 1986.

Merle, O. and Michon, L.: The formation of the West European rift: a new model as exemplified by the Massif Central area, B. Soc. Géol. Fr., 172, 213–221, 2001.

Misra, S., Mandal, N., and Chakraborty, C.: Formation of Riedel shear fractures in granular materials: Findings from analogue shear experiments and theoretical analyses, Tectonophysics, 471, 253–259, 2009.

Morimoto, N.: Nomenclature of pyroxenes, Mineral. J., 14, 198–221, 1989.

Paterson, S. R., Fowler Jr., T. K., Schmidt, K. L., Yoshinobu, A. S., Yuan, E. S., and Miller, R. B.: Interpreting magmatic fabric patterns in plutons, Lithos, 44, 53–82, 1998.

Petford, N.: Which effective viscosity?, Mineral. Mag., 73, 167–191, 2009.

Picard, D., Arbaret, L., Pichavant, M., Champallier, R., and Launeau, P.: Rheology and microstructure of experimentally deformed plagioclase suspensions, Geology, 39, 747–750, 2011.

Philpotts, A. R. and Ague, J. J.: Principles of Igneous and Metamorphic Petrology, Cambridge University Press., 667 pp., 2009.

Saint Martin, M.: Carte géologique harmonisée du département de l'Ardèche, BRGM/RP-57097-FR, 423 pp., 2009.

Smith, J. V.: Ductile-brittle transition structures in the basal shear zone of a rhyolite lava flow, eastern Australia, J. Volcanol. Geoth. Res., 72, 217–223, 1996.

Smith, J. V.: Shear thickening dilatancy in crystal-rich flows, J. Volcanol. Geoth. Res., 79, 1–8, 1997.

Smith, J. V.: Structural analysis of flow related textures in laves, Earth-Sci. Rev., 57, 279–297, 2002.

Tchalenko, J. S.: The evolution of kink-bands and the development of compression textures in sheared clays, Tectonophysics, 6, 159–174, 1968.

Vernon, R. H.: Review of microstructural evidence of magmatic and solid-state flow, Visual Geosciences, 5, 1–23, 2000.

Vigneresse, J. L., Barbey, P., and Cuney, M.: Rheological transitions during partial melting and crystallization with application to felsic magma segregation and transfer, J. Petrol., 37, 1579–1600, 1996.

Ward, K. M., Zandt, G., Beck, S. L., Christensen, D. H., and McFarlin, H.: Seismic imaging of the magmatic underpinnings beneath the Altiplano-Puna volcanic complex from the joint inversion of surface wave dispersion and receiver functions, Earth Planet. Sc. Lett., 404, 43–53, 2014.

Walters, J. B.: MinPlot: A mineral formula recalculation and plotting program for electron probe microanalysis, Mineralogia, 53, 51–66, 2022.

Warr, L. N.: IMA–CNMNC approved mineral symbols, Mineral. Mag., 85, 291–320, 2021.

Westerman, D., Rocchi, S., Breitkreuz, C., Stevenson, C., and Wilson, P.: Structures related to the emplacement of shallow-level intrusions, in: Physical Geology of Shallow Magmatic Systems, Springer, Cham., 83–118, https://doi.org/10.1007/11157_2017_31, 2017.